

# REFLECTANCE SPECTRA OF EARTH-LIKE EXOPLANETS

Dissertation  
zur Erlangung des Doktorgrades  
des Department Physik  
der Universität Hamburg

vorgelegt von  
**Mariana Wagner**  
aus Lübeck

Hamburg  
2011

Gutachter der Dissertation:	Prof. Dr. Peter H. Hauschildt Prof. Dr. Stefan Dreizler
Gutachter der Disputation:	Prof. Dr. Dieter Horns Prof. Dr. Jürgen Schmitt
Datum der Disputation:	8. Juni 2011
Vorsitzender des Prüfungsausschusses:	Dr. Robert Baade
Vorsitzender des Promotionsausschusses:	Prof. Dr. Günter Huber
Dekan des Fachbereichs Physik:	Prof. Dr. Heinrich Graener

## ZUSAMMENFASSUNG

Im Rahmen dieser Arbeit wird eine neue untere Randbedingung zur Berechnung planetarer Atmosphären in PHOENIX Modelle implementiert, die es ermöglicht, Reflektionsspektren erdähnlicher Planeten mit optisch dünnen Atmosphären zu modellieren. Hierbei stehen besonders diejenigen extrasolaren Planeten im Fokus, die sich in der habitablen Zone ihres Muttersterns befinden und Leben hervorbringen könnten. Hat der Planet eine optisch dünne Atmosphäre, so wird das reflektierte Licht Informationen über die Beschaffenheit der Planetenoberfläche enthalten. Besonders bei denjenigen Planeten, die nur einen einzigen Oberflächentyp besitzen (z.B. Wüste), sind diese Signaturen gut zu erkennen. Die neue untere Randbedingung beinhaltet die Behandlung von Oberflächen wellenlängenunabhängiger und winkel- oder wellenlängenabhängiger Albedos. So konnten erdähnliche Exoplaneten mit Wasser-, Wald-, Wüsten- oder Schneeoberfläche nachgebildet und berechnet werden. Neben diesen Objekten wurden auch Planeten mit optisch dicken Atmosphären und unterschiedlichen chemischen Zusammensetzungen simuliert und so Reflektionsspektren der Venus, der Supererde GJ 1214b und einer Gliese 581g-ähnlichen Supererde berechnet.

## ABSTRACT

Within this thesis a new lower boundary condition is implemented into the PHOENIX code in order to model reflectance spectra of Earth-like exoplanets with optically thin atmospheres with an emphasis on those objects that orbit their host star within the habitable zone. In case of optically thin atmospheres, the reflected light can contain information about the planetary surface. Especially for those exoplanets that are covered by a single surface type only, these surface signatures can be distinctive. The new lower boundary condition allows the treatment of wavelength-independent, angular dependent and wavelength dependent surface albedos. The simulated objects span terrestrial exoplanets like an ocean world, a snowball-, desert or jungle planet. In addition, planets with optically thick atmospheres and of different chemical composition have been modeled. The simulations also include a Venus-like planet, the super-Earth GJ 1214b and a Gliese 581g-like super-Earth.



# Contents

<b>1</b>	<b>INTRODUCTION</b>	<b>1</b>
<b>2</b>	<b>EXOPLANETS - AN OVERVIEW</b>	<b>5</b>
2.1	HABITABLE EARTH-LIKE PLANETS . . . . .	9
2.2	SPECTRAL FINGERPRINTS & BIOMARKERS . . . . .	11
2.3	EVOLUTION OF THE ATMOSPHERE . . . . .	13
<b>3</b>	<b>IRRADIATED PLANETARY ATMOSPHERES</b>	<b>17</b>
3.1	THE PHOENIX MODEL ATMOSPHERE CODE . . . . .	17
3.1.1	UPPER BOUNDARY CONDITION . . . . .	21
3.1.2	LOWER BOUNDARY CONDITION / ALBEDO . . . . .	22
<b>4</b>	<b>RADIATIVE TRANSFER</b>	<b>29</b>
4.1	OPERATOR SPLITTING METHOD . . . . .	32
4.2	MODIFICATIONS TO THE $\Lambda^*$ -OPERATOR . . . . .	33
4.3	TEMPERATURE CORRECTION . . . . .	37
4.4	MODIFICATIONS TO THE TEMPERATURE CORRECTION . . . . .	40
<b>5</b>	<b>RESULTS</b>	<b>42</b>
5.1	GRAY EARTHS . . . . .	44
5.2	THE EARTH-LIKE ATMOSPHERE . . . . .	45
5.2.1	THE THIRD ATMOSPHERE . . . . .	45
5.2.2	THE SECOND ATMOSPHERE . . . . .	48
5.2.3	THE FIRST ATMOSPHERE . . . . .	50
5.3	THE VENUS-LIKE ATMOSPHERE . . . . .	52
5.4	HYPOTHETICAL SUPER-EARTH . . . . .	55
5.5	STEAMY WORLD GJ1214 b . . . . .	57
5.6	OCEAN PLANET . . . . .	59

5.7	SNOWBALL PLANET . . . . .	61
5.8	DESERT (MARTIAN) PLANET . . . . .	63
5.9	JUNGLE PLANET . . . . .	65
<b>6</b>	<b>PHOTOMETRY</b>	<b>67</b>
<b>7</b>	<b>SUMMARY &amp; OUTLOOK</b>	<b>71</b>

---

# Chapter 1

## INTRODUCTION

The number of detected extrasolar planets is rising rapidly. The very first exoplanet ever detected is PSR B1257+12B, a super-earth mass planet orbiting the distant pulsar PSR 1257+12. Just three years later in 1995, the first extrasolar planet orbiting a main sequence star was found. A cascade of further detections began. Today, over 530 exoplanets are listed in the “extrasolar planets encyclopedia” (<http://exoplanet.eu/>). So far, the radial velocity method has proven to be the most successful way to discover new exoplanets. Since this method is measuring the perturbation of the host star’s motion due to a companion, it favors the discovery of close-in high-mass planets like hot Jupiters, and thus worlds hostile to life. After a decade that was rich in giant exoplanet detections, the space observatory COROT (launch December 2006) and Kepler (March 2009) are now searching for smaller worlds.

There are a number of missions planned in order to detect and characterize exoplanets, most of them using transit spectroscopy. Among them are the PLATO mission and the James Webb Space Telescope. If an atmosphere is present, the information received by transmission spectra are diagnostics of the temperature and chemical composition of these atmospheres (Seager et al. (2000)) and provide an insight into the nature of the exoplanet. But unfortunately, direct observations and, therefore, reflectance spectra of extrasolar planets are not yet feasible. Direct characterization would provide information about the planet’s size, atmospheric gas constituents, total atmospheric column density, clouds and surface properties. This would allow an instantaneous evaluation in terms of habitability. Habitability is indicated by the presence of spectral features we consider to be biogenic. These biomarkers- and signatures are determined by life as we know it and this life is carbon based and needs water as a solvent. A planet able to develop life must meet a lot of requirements. Even if we really find a second Earth, it might be in the wrong stage of evolution and no signs of life might show up in the measurements.

The exoplanetary status report of 2010 by Lammer et al. (2010) claims that assuming a non rising budget for future space missions, it would be unlikely that there will be a space mission before 2020 solely designed for the direct characterization of exoplanet atmospheres. But as this is the next step in the detection of possibly life-bearing worlds, there is a rising need for theoretical assistance in order to give input to the design of this first generation of new instruments and to understand what we will see with them.

In the framework of this thesis I have simulated reflectance spectra of exoplanets that are of Earth and super-Earth sizes focussing on those objects with optically thin atmospheres. Those planets were given different surface types with corresponding atmospheres above them. The modeled objects span a variety of planets like an Earth-twin around a Sun-like star in different stages of its evolution, a martian-like desert planet, an ocean world, a snowball planet and super-Earths with the parameters of GJ 1214b and the hypothetical Gliese 581g. The models were calculated using the PHOENIX code developed by Hauschildt et al. (2008). The atmosphere is build and the radiative transfer is solved in an iterative process, thus PHOENIX allows a self consistent treatment. All calculations are done in 1D spherical symmetry. Giving the planet a specific surface and allowing irradiation to be partly absorbed and partly reflected depending on the albedo requires to adjust the lower boundary condition. In this way it is possible to simulate soils that have a wavelength dependent reflection coefficient or, e.g., a vegetated surface as well as liquid or gray surfaces.

---

## DISSERTATION OUTLINE

This thesis is organized as follows: A brief overview on the topic of exoplanets is given in chapter 2. The constraints that a planet has to fulfill in order to develop and harbor life will be discussed in section 2.1. When life is present, it adds signatures to the planet's transmission or reflectance spectrum, called "spectral fingerprints". However, the biosignatures or biomarkers we are searching for are determined by the life as we know it (2.2). But Earth's spectral signature has changed over time, therefore a closer look on possible evolutionary stages of an Earth-like planet can be found in chapter 2.3.

The basic theory of modeling exoplanetary irradiated atmospheres is introduced in chapter 3, starting with the description of our model code PHOENIX (chapter 3.1). The boundary conditions to model irradiation at the upper boundary and various types of reflection (and thus albedos) at the lower boundary are explained in section 3.1.1 and 3.1.2. A brief guide to the radiative transfer (RT) method is presented in chapter 4. Calculating an optically thin atmosphere over a solid core that is able to absorb parts of the incoming radiation depending on its surface albedo requires a modification to the  $\Lambda^*$ -operator that solves the RT. These changes are explained in chapter 4.1. Also the way the energy conservation is handled differs when treating a very thin atmosphere over a solid (energy storing) core (chapter 4.3).

The results will be discussed in chapter 5. Those are: Earth's atmosphere in its different evolutionary stages (5.2), Venus (5.3), the hypothetical Gliese 581g (5.4) and GJ 1214b (5.5). All these scenarios represent models with a wavelength independent fixed gray albedo. Wavelength and angular dependent reflectance spectra that would result from an ocean, a snowball, a desert or a jungle planet are the topic of chapters 5.6 to 5.9.

A suggestion for filter ranges that would be needed to detect dominant surface features, inspired by the filters of the NIRSpec onboard the James Webb Space Telescope, is made in chapter 6. Finally, a summary and outlook is provided in chapter 7.



---

## Chapter 2

# EXOPLANETS - AN OVERVIEW

The first approach to understand planets in other systems is to take a look at the planets closest to us. We classify exoplanets by the guidelines that are provided by our own Solar System, differentiating by the mass of the objects (see figure 2.1). Hot Jupiters are heavy objects with masses close to Jupiter or larger ( $1.9 \cdot 10^{27}$  kg or  $318 \cdot M_{\text{Earth}}$ ). They are the type of exoplanet that is most likely to be detected since most of the recent observational techniques favor the detection of high mass objects. The Neptune class includes objects of about  $17 \cdot M_{\text{Earth}}$ . Neptune orbits the Sun at 30 AU distance, the so called “hot neptunes” are closer in. The system of Gliese 436, e.g., consists of a single Neptune-mass planet in a short-period orbit around a red dwarf star. “Super-Earths” are bridging the gap in mass between the Neptunes and Earth-like objects. A representative of this class of planets is e.g. GJ 1214b, that will be discussed in detail in chapter 5.13. On the lowest end of the mass range are Earth analogues with solid rocky cores.

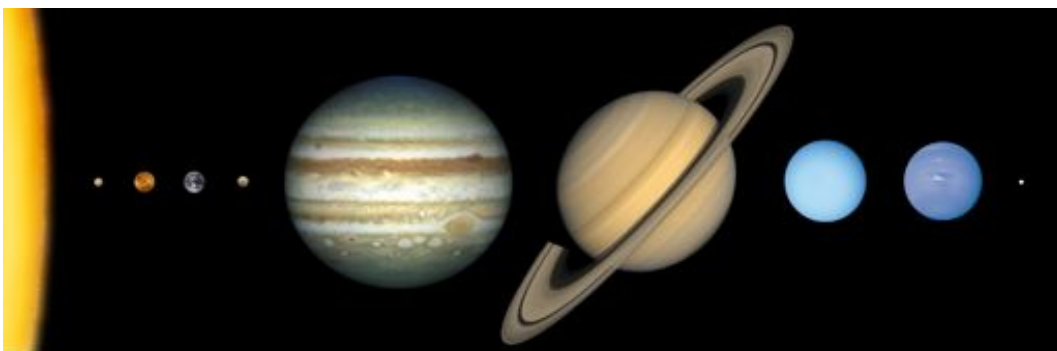


Figure 2.1: *The Solar System planet serve as a measure to characterize exoplanets. We differentiate among (hot) Jupiters, (hot) Neptunes and Earth-like planets, inserting the so-called “super-Earth” in between the mass range of Neptune and Earth. Picture: Courtesy NASA/Lunar & Planetary Lab*

An exoplanet is very faint compared to its host star. To set an example, the Earth-Sun brightness ratio is about  $10^{-10}$  in the visible light and about  $10^{-7}$  in the thermal infrared. But as we go to cooler stars, such as red dwarfs, the contrast ratio between a terrestrial companion and its host star decreases, making those small stars interesting targets for observations. On the ground the M<sub>Earth</sub> Project photometrically monitors 2000 nearby M dwarfs in order to find super-Earths within the habitable zone. The team around David Charbonneau (Nutzman & Charbonneau (2008)) had their greatest success with this instrument so far in finding the previously mentioned super-Earth GJ 1214b.

Missions in space that are dedicated to the detection of exoplanets are CoRoT and Kepler. The CoRoT space observatory, that just recently found the low mass exoplanet CoRoT 7b with  $1.65 \cdot M_{\text{Earth}}$ , was successfully launched on December 27 from the Baikonour Cosmodrome and started observations in February 2007. Kepler is a 0.95 m diameter telescope launched in March 2009. Among others, one of Kepler's mission goals is the determination of the percentage of terrestrial and larger planets that are in or near the habitable zone of a wide variety of stars. Kepler simultaneously monitors the brightnesses of more than 100 000 stars during its mission life time of about 3.5 years.

Planet candidates are confirmed by radial velocity measurements from the ground using e.g. the HARPS and CORALIE spectrograph in La Silla, the SOPHIE spectrograph in the Observatoire de Haute Provence, the UVES and FLAMES spectrographs in Chile or the Coudé-Echelle spectrograph in Tautenburg. Ground based observatories able to perform direct imaging of extrasolar planets orbiting nearby stars are, e.g., the Spectro-Polarimetric High-contrast Exoplanet Research (SPHERE) at the VLT and the High Contrast Instrument for the Subaru Next Generation Adaptive Optics (HiCIAO) at the Subaru telescope and finally the Gemini Planet Imager (GPI) at the Gemini telescope.

Future missions dedicated to the detection and characterization of exoplanets are e.g. the James Webb Space Telescope (JWST), currently constructed by ESA/NASA and scheduled for launch in 2014. JWST uses the transit method and will bring new information about atmospheric constituents of exoplanetary atmospheres. The Terrestrial Planet Finder (TPF) is a concept that involves a coronagraph operating at visible wavelengths and a large-baseline interferometer operating in the infrared. It is designed to study planet formation and development in disks of dust and gas around newly forming stars as well as taking spectra of terrestrial exoplanets. However, TPF is not planned to be launched in the near future.

Observations of transits, combined with radial velocity information can provide estimates of the mass and radius of the planet, the brightness temperature and atmospheric absorption features (Swain et al. (2008)). The temperature and the radius allow a first estimate

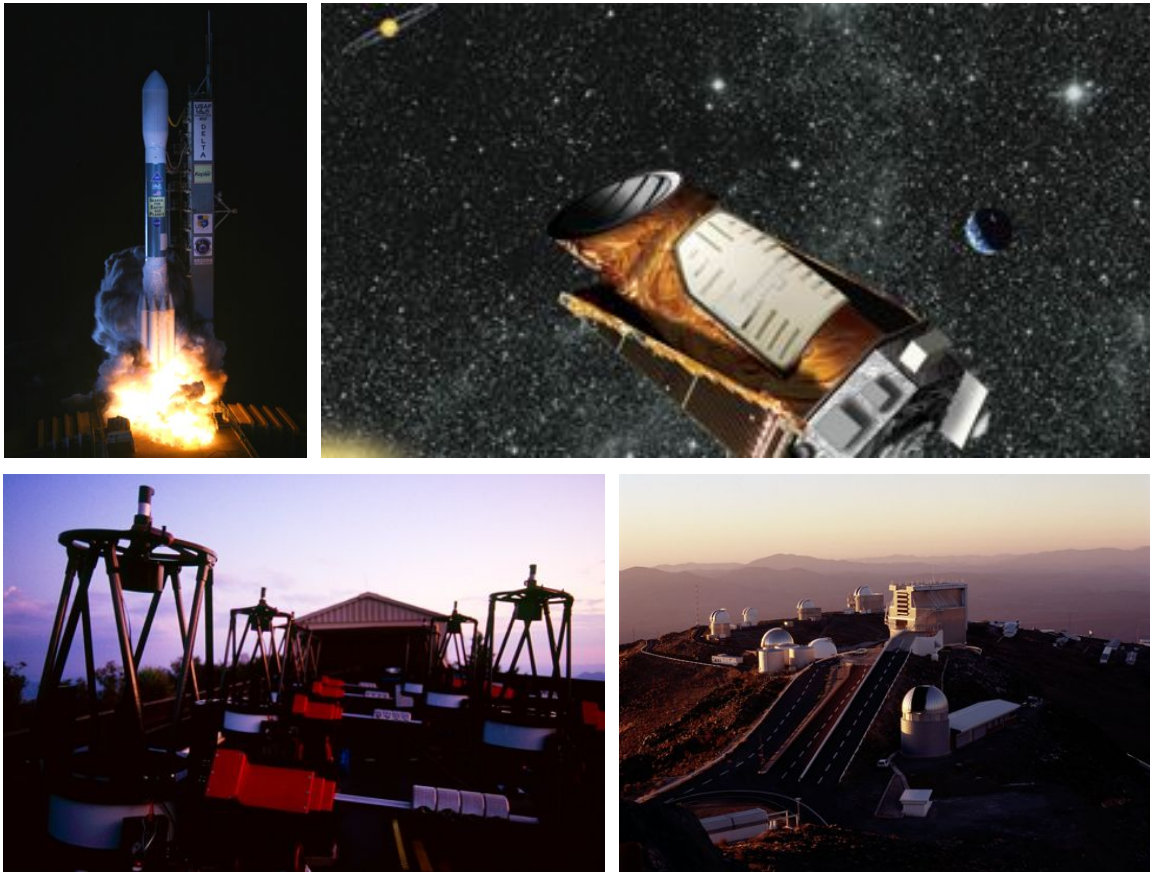


Figure 2.2: *The Kepler space observatory was launched in 2009 and will monitor a large set of stars in order to find exoplanets within the habitable zone. MEarth is a project of the Harvard-Smithsonian Center for Astrophysics (CfA) and monitors the sky for planets around M-stars. The right picture in the lower row shows the La Silla observatory in Chile. Image sources: NASA, [www.cfa.harvard.edu](http://www.cfa.harvard.edu) & [farawayworlds.files.wordpress.com](http://farawayworlds.files.wordpress.com)*

of the general physical and chemical processes on the planet. In the future, once we are able to measure the emitted or reflected photons by the planet itself, we could directly determine the size, temperature, albedo, atmospheric composition, cloud coverage and surface properties. This will mean a huge improvement in the characterization of objects in terms of their habitability. Coronagraphic imaging in the visible light and interferometric imaging (thermal infrared) are direct observational techniques that would provide these informations (Kaltenegger et al. (2002)).

Atmospheric modeling is needed to gain an insight into the basic properties of those atmospheres and to add to the instrumental design of future missions. The atmosphere holds the key to understand an exoplanet's nature and is crucial for the development of

habitability. We can receive spectral information if the planet transit its host star. During primary eclipse, i.e. when the planet is crossing the stellar disk, the stellar spectrum picks up features of the planet's atmosphere, leading to a combined spectrum. Briefly before the planet is covered by the star during secondary eclipse, the stellar light is reflected by the planet's dayside and produces the reflectance spectrum. Both, transmission and reflectance spectra contain information about the planets atmospheric composition but if the atmosphere is optically thin, the reflectance spectrum also contains features of the surface. Such a well observed and understood spectrum for comparison is provided by our Earth in the form of Earthshine spectra . "Earthshine" or "planetshine" is daylight that is retro-reflected from the Moon's nightside. Spectral features in Earth's spectrum that are assigned to life as we know it set the standard for what we define to be bioindicators or even biomarkers. But even if we find a second Earth, it could still be in another stage in its evolution (chapter 2.3) and we have to consider that too when interpreting what we see.

Thus it is important to develop numerical models to complement the upcoming and ongoing observations. Several groups have modeled exoplanetary atmospheres (Segura et al. (2003), Grenfell et al. (2007), Kaltenegger & Traub (2009) or Meadows (2006)).

## 2.1 HABITABLE EARTH-LIKE PLANETS

A planet has to satisfy a lot of constraints in order to develop and harbor life as we know it. Beginning at the largest scale, its host star has to be located within the galactic habitable zone (Lineweaver et al. (2004)). Furthermore the planet has to orbit its host star at a distance that allows water to exist in liquid form, the habitable zone (HZ) (Kasting et al. (1993)). The inner edge of the HZ is determined by water loss via photolysis and hydrogen escape. According to Kasting the HZ ends at the stellar distance where  $\text{CO}_2$  cloud formation sets in. This would cause a high albedo and subsequent glaciation. There is also a converse theory claiming that those clouds could warm the surface, extending the outer edge of the HZ. Not every star is a good host star. Stars with a spectral class earlier than A do not qualify to host habitable worlds because they are evolving too fast. According to Kasting “mid- to early-K and G stars may therefore be optimal for the development of life”.

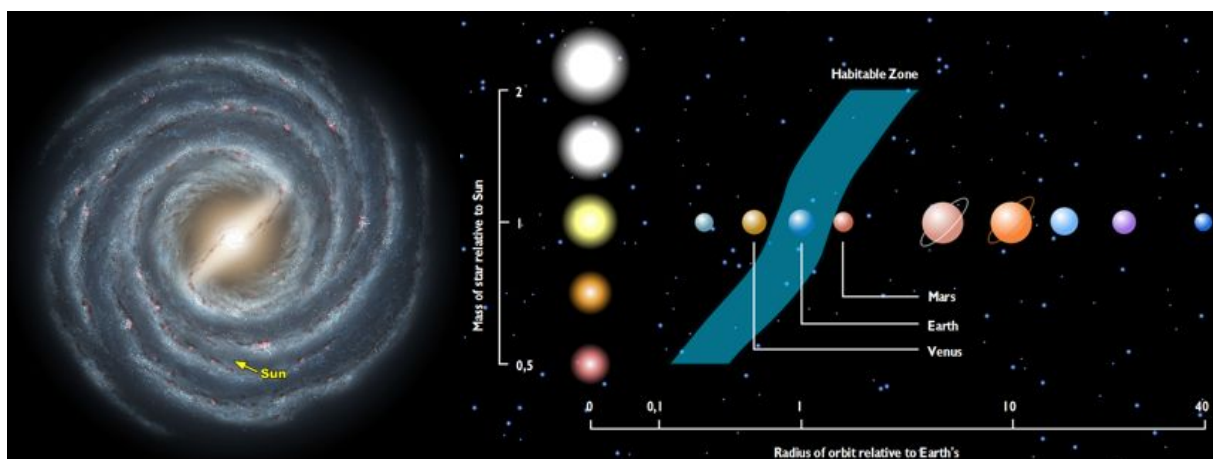


Figure 2.3: *Left-hand picture shows our position within the galaxy. On the right-hand side heliocentric distances for different planets and host star sizes are shown. Pictures taken from [www.astrobio.net](http://www.astrobio.net).*

Provided the planet orbits within the HZ, it shouldn't be too big or too small. A small planet suffers a low gravity and is not able to keep its atmosphere. Small planets lose their energy quickly and are therefore known to lack plate tectonics, which are essential for the development of life. The upper mass limit is given by the fact that too big planets attract light gases and become gas giants. Projected onto Earth's orbit the planets mass should range in between  $0.5 - 10M_{\text{Earth}}$ . If the planet is in the right orbit and of the right size, the planets rotation, atmospheric convection, clouds and surface texture become important.

Our Earth has a tilted rotation axis. This tilt of  $23.4^\circ$  is stabilized by the presence of Moon and enables our climate system to be as mild as we know it. A non-tilted rotation axis would cause the climate to be extreme and would probably have supported other forms of life to develop. Also planets on eccentric orbits are likely to have extreme climate with large seasonal variations, e.g. an ocean world at periastron could become a snowball at apoastron (Spiegel et al. (2008)).

In 1961, Frank Drake formulated an equation to estimate the number of detectable extraterrestrial civilizations in the Milky Way. It takes into account the fraction of habitable planets that might develop intelligent life and the timescales on which those civilizations might send out signs into space<sup>1</sup>.

What signature does life have? The search for life requires a definition of what we consider to be “life”. The definition provided by Leger et al. (1996) is as follows: Life ..

- contains information
- is able to replicate itself
- undergoes random changes in its information package that allow Darwinian evolution to proceed

Apart from the classical biomarkers that will be introduced in the next chapter, it should just be mentioned here that life can also exist in more cryptic forms. Organisms can adapt to a wide range of environments like Hypoliths (organisms on the underside of rocks that are not totally opaque), soil and desert organisms (living within sands and soils loose or building crusts) or the ones living in salt crusts or ice. Cockell et al. (2009) calculated that those photosynthetic organisms could build up today's oxygen concentration on Earth within 1.3 Ga, assuming there are not too many sinks for oxygen.

---

<sup>1</sup>([seti.org/drakeequation](http://seti.org/drakeequation))

## 2.2 SPECTRAL FINGERPRINTS & BIOMARKERS

The reflectance or transmission spectrum of a planet contains information about the composition of the atmosphere. The absorption lines or bands thus serve as “fingerprints” of the main chemical constituents and reveal potential habitability. The main bioindicators in Earth’s atmosphere are molecular oxygen ( $O_2$ ), ozone ( $O_3$ ), methane ( $CH_4$ ), nitrous oxide ( $N_2O$ ), water ( $H_2O$ ) and carbon dioxide ( $CO_2$ ). Water and carbon dioxide serve as the main greenhouse gases in our atmosphere.

When searching for signatures in spectra that allow us to determine whether a planet bears life or not, it is useful to distinguish between bioindicators and biomarkers. For example methane can be of biological or non-biological origin, therefore it can be labeled as a “bioindicator”, whereas a “biomarker” is a feature that can definitely be assigned to biological origin. Reliable biomarkers in Earth’s atmosphere would be the vegetation red edge (will be explained later) and  $N_2O$ , since the only source known to produce nitrous oxide in abundance are anaerobic denitrifying bacteria (Des Marais et al. (2001)). Most of the nitrous oxide is produced in the ground or in the oxygen-deficient regions in the ocean, in depths of over 130 m. The  $N_2O$  bands are hard to detect and beyond that overlapped by  $CH_4$ ,  $CO_2$  and  $H_2O$  (Kaltenegger & Selsis (2009)).

Methane is also a very efficient greenhouse gas and can either be produced by life, by degradation of organic debris or by geologic processes. Microorganisms produce a large amount of methane when organic matter decays in oxygen-free environments in the process of methanogenesis. Methane could build up to higher levels in the atmosphere in the absence of oxygen but it needs to be refilled constantly due to its destruction by photooxidation. The abiotic (geological) source of methane is volcanism, the Earth’s crust contains huge amounts of methane. Methane emerging from the ocean floor is exposed to high pressures and low temperatures and forms methane ice.

Ozone is produced by a photochemical reaction that takes place in the stratosphere. The UV light (shorter than 242 nm) photolyzes  $O_2$  molecules and the single oxygen atoms can now react with other oxygen molecules to form ozone. It is photodissociated again above the troposphere by visible and longer UV radiation. The code used in this work (PHOENIX) is calculating the atmospheric abundances in chemical equilibrium (concentrations of the reactants have no net change over time), but does not include photochemical reactions. This is why we can not reproduce an ozone layer and spectral signature as present on Earth and do not receive a temperature inversion in the stratosphere, which is a result of the absorption of UV light by the ozone layer. Leger et al. (1996) investigated

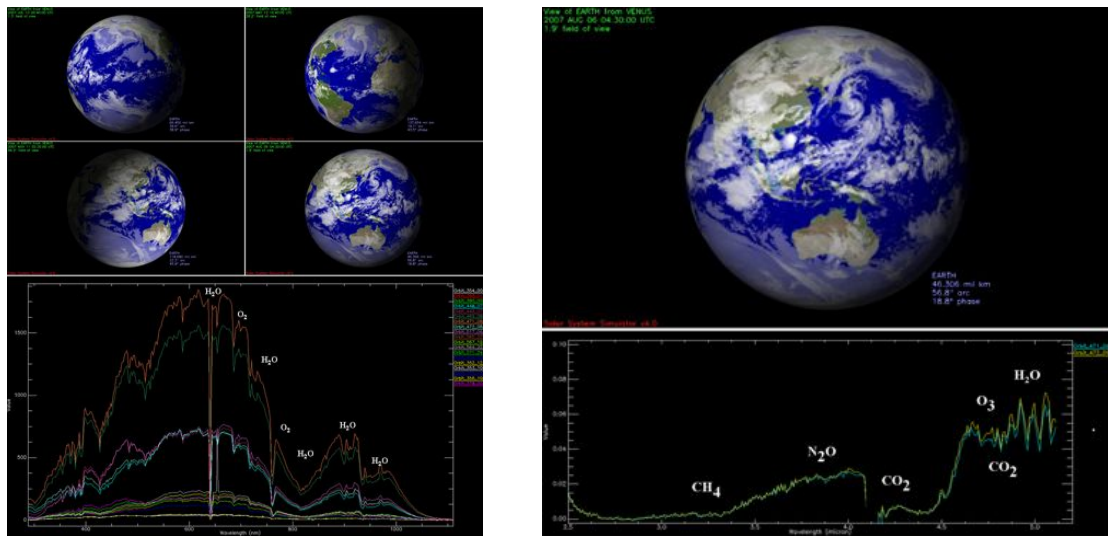


Figure 2.4: *The Earth as seen from the VIRTIS instrument on Venus Express. Both pictures taken from ESA/VIRTIS/INAF-IASF/Obs. de Paris-LESIA (Earth views: Solar System Simulator JPL-NASA).*

$O_3$  as a tracer for  $O_2$ . Its most dominant feature is the strong absorption band at  $9.6\mu m$ , this band is highly saturated but still it is a good indicator for the existence of traces of oxygen.

In case of Earth,  $O_2$  is produced mainly by the biosphere. As  $O_2$  is highly reactive it would vanish in a few million years, if not refilled by the biosphere (Kaltenegger et al. (2002)). In other systems it may also result from abiotic reactions. Those are the photolysis of water with subsequent escape of hydrogen to space and the photolysis of carbon dioxide with subsequent recombination and formation of molecular oxygen. But this atmospheric oxygen has a limited lifetime due to loss to space and the oxidation of the planets crust.

If signatures of single bioindicators can be found in exoplanetary atmospheres, they could also be interpreted as false positives (see Selsis (2002) for further details). To avoid false positive detections it is, therefore, more advisable to search for a combination of signatures, ideally  $H_2O$ ,  $O_3$ ,  $O_2$  and  $CH_4$  in the visible and  $CO_2$ ,  $H_2O$ ,  $O_3$ ,  $H_2O$  and  $CH_4$  in the thermal infrared. But even this can just be taken as a measure of potential habitability and not as a proof.

The ultimate biomarker for life as we know it is the vegetation red edge (VRE) caused by chlorophyll (figure 2.5). Chlorophyll (a and b) absorbs in the blue (400-500 nm) and red (600-700 nm) part of the visible spectrum. In between the reflectance increases, causing the plants to appear green. In the near infrared around  $0.725\mu m$  reflectance increases

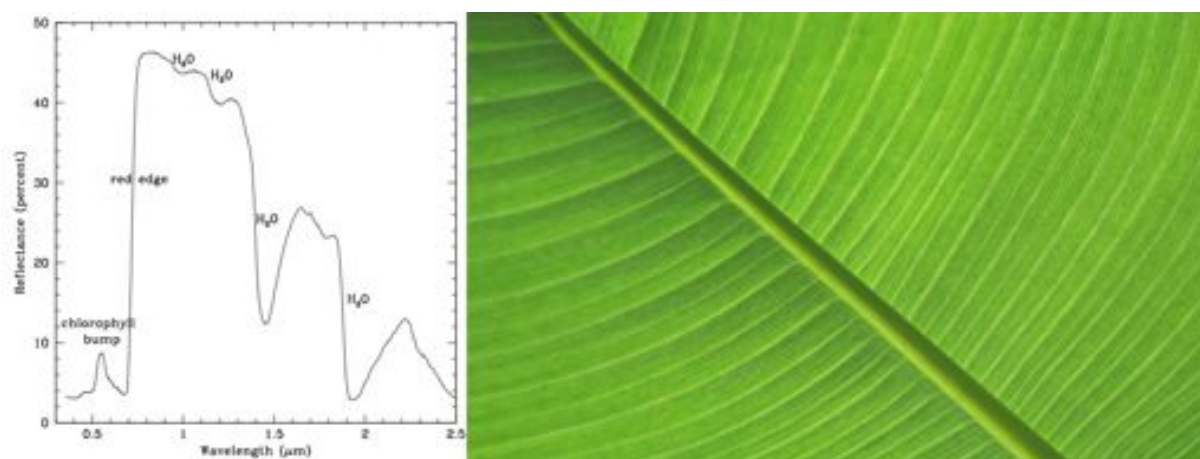


Figure 2.5: *The sharp rise in reflectance, the vegetation red edge (Image credit: blogs.discovermagazine.com) caused by chlorophyll in photosynthetic plants (Image credit: travelphoto.net)*

steeply. This rise in reflectance is called the “red edge” and ensures a cooling of the plants and thus the loss of chlorophyll. In 2007, Venus Express took spectra of the Earth from a distance of  $62 - 175 \cdot 10^6$  km and could find water and molecular oxygen in Earth’s atmosphere in the visible light but not the VRE, see figure 2.4.

## 2.3 EVOLUTION OF THE ATMOSPHERE

The signatures of bioindicators and biomarkers on Earth have changed throughout geological timescales. Even if we found a second Earth, it still might be in a different stage of its evolution, e.g. prior to developing life and thus not showing biosignatures in its spectrum. Again, the only proxy to study atmospheric evolution of a habitable planet is given by the Earth itself. The different stages of atmospheric evolution can be roughly divided into a three epochs. Kaltenegger et al. (2006b) subdivides it into five. Based on the chemical mixing ratios given in their paper, I chose to model three evolutionary stages, which I will further denote as first, second and third atmosphere, with the third atmosphere being our present one.

The Earth is 4.6 billion years old, formed by accretion of solid materials that condensed from the solar nebula. The volatile compounds of those planetesimals and the release of volatiles from the interior were the basic components of the initial atmosphere. During



Figure 2.6: *On the left: an artists impression of the Earth during the heavy bombardment period. Right: The third atmosphere as we know it today. (Image credit: NASA)*

the time of large impact events the atmospheric composition was dominated by carbon dioxide, nitrogen, methane, ammonia, sulphur dioxide, hydrochloric acid and oxygen (Kaltenegger et al. (2006a)). Earth's surface was molten, maybe covered by an unstable crust, the temperature far too high to allow water to exist in a liquid state. Water could accumulate in abundance being brought in by comets and larger objects like Mercury-sized planetary embryos that formed in the asteroid belt beyond 2.5 AU. In the accretion phase, oceans formed and were repeatedly vaporized again by impacts. This stopped about 3.8 Ga ago with the end of the late heavy bombardment period, the surface heat flux faded and the atmosphere finally rained out into a stable ocean (Kasting (1993)). The faint young sun paradox should be mentioned here. About 4 Ga ago, the Sun was approximately 30% less luminous. Even in the presence of greenhouse gases with the predicted concentrations, the surface temperature would have dropped below the freezing point of water, preventing the evolution of life. Kasting (1993) suggests a higher concentration of the greenhouse gases carbon dioxide and methane.

## THE FIRST ATMOSPHERE

The first atmosphere formed about 3.9-3.8 Ga ago. The atmosphere consists of nearly 90% nitrogen, 10% carbon dioxide and 1.79 ppm methane (other molecules are neglected), as suggested by Kaltenegger et al. (2006a).

## THE SECOND ATMOSPHERE

About 2.4 Ga ago, the carbon dioxide levels decreased by sedimentation and weathering. The first kind of life occurred in form of a methanogenetic bacteria, called “methanogens”. Those are very basic and archaic bacteria, the only kind of archaea that use carbon dioxide to gain energy in the process of methanogenesis. This early form of life created high levels of methane in the atmosphere. Methane as an efficient greenhouse gas raised the temperature providing these kinds of bacteria even better living conditions. The limiting factor was apparently an organic haze forming at  $\text{CH}_4/\text{CO}_2 = 1$ , creating an anti-greenhouse effect. The first kind of photosynthetic bacteria evolved. Those cyanobacteria added oxygen to the atmosphere, which is toxic to the methanogens, saving the atmosphere from further warming (Kasting & Catling (2003)).



Figure 2.7: *Left: Cyanobacteria, the first kind of photosynthetic life form on Earth. Right: Methanogens are living in extreme habitats, e.g. around black smokers at about 400 K. Picture sources: cleantechnica.com & marum.de.*

## THE THIRD ATMOSPHERE

The major increase in levels of oxygen occurred between 2.3 Ga and 0.8 Ga ago, based on the analysis of ancient soils (paleosols). With the rise of oxygen, the ozone layer started to form in the upper atmosphere, giving some shielding from UV radiation to the emerging life. Phytoplankton in the ocean added its signature to the spectrum. 440 million years ago the surface was conquered by plants and finally the vegetation red edge (VRE) occurred in the spectrum.

The two most important greenhouse gases in our present atmosphere are water vapor (contributing 2/3 of the greenhouse warming) and carbon dioxide (1/3). Methane, ozone and nitrous oxide contribute another 2 – 3%. The incoming visible and nIR radiation is stored within the ground which re-emits in the infrared. But this outgoing IR radiation is again re-emitted by greenhouse gases within the atmosphere. Without the greenhouse effect Earth would be on average about 33 K cooler.

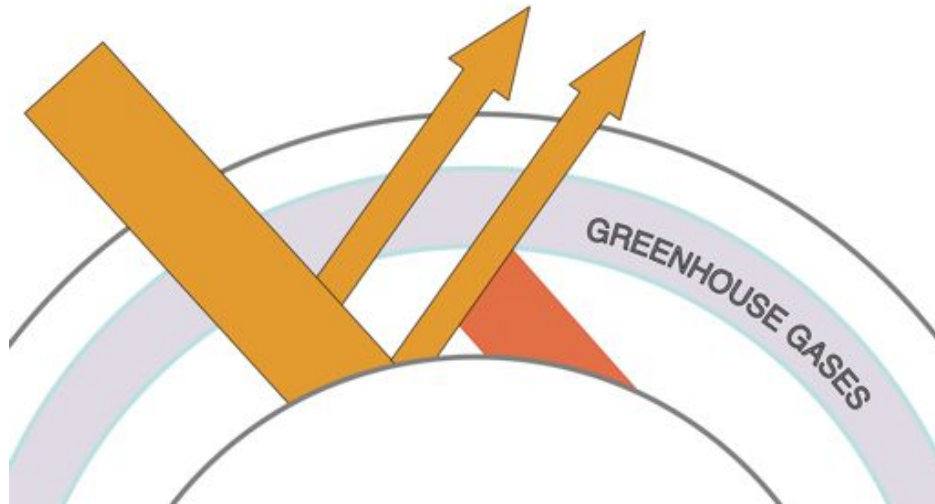


Figure 2.8: *On Earth the main greenhouse gases are water vapor and carbon dioxide. They absorb and emit radiation within the thermal infrared range.*

Today, our atmosphere consists of five layers, the troposphere (from the surface up to 6-17 km), the stratosphere (up to  $\sim 51$  km), the mesosphere (up to 80-85 km), the thermosphere (ranges up to the exobase) and finally the exosphere (varies strongly with solar activity  $\rightarrow$  350-800 km). Those main layers are determined by the in- or decrease of the temperature with altitude. The lowest layer, the troposphere, is heated mainly by the surface. The incoming solar radiation is partly absorbed and reradiated at larger wavelengths (in the infrared) and partly reflected. The amount of reflected radiation depends for an optically thin atmosphere on the surface albedo. The temperature decreases from the surface upwards within the thermosphere, increases in the stratosphere and decreases again in the mesosphere. The temperature increase within the stratosphere is caused by the absorption of ultraviolet sunlight by the ozone layer. The results of the simulations for atmosphere 1-3 can be found in chapters 5.2.3 to 5.2.1.

---

## Chapter 3

# IRRADIATED PLANETARY ATMOSPHERES

### 3.1 THE PHOENIX MODEL ATMOSPHERE CODE

“PHOENIX is a general-purpose state-of-the-art stellar and planetary atmosphere code. It can calculate atmospheres and spectra of stars all across the HR-diagram including main sequence stars, giants, white dwarfs, stars with winds, T Tauri stars, novae, supernovae, brown dwarfs and extrasolar giant planets<sup>1</sup>”.

The general assumptions for the 1D planetary model are:

- 1D spherical symmetry
- Hydrostatic equilibrium
- Statistical equilibrium (time-independent atmosphere)
- Energy conservation (no sources and sinks)
- Energy transport only via radiation (no convection)
- Local thermodynamic equilibrium (LTE)

The 1D spherically symmetric PHOENIX model atmosphere of a rocky exoplanet consists of a fixed number of atmospheric shells or layers. The setup is shown in figure 3.1. Each layer holds its own set of thermodynamic variables. The host star’s impinging radiation is

---

<sup>1</sup>cited from: [www.hs.uni-hamburg.de/EN/For/ThA/phoenix/index.html](http://www.hs.uni-hamburg.de/EN/For/ThA/phoenix/index.html)

represented by the boundary condition at the outermost atmospheric shell, the innermost layer serves as the planet’s solid surface. This lower boundary has to allow parts of the incoming energy to be stored within the ground and the rest to be reflected. This is one of the major changes that had to be done within this work in order to model planets with a rocky core. Both boundary conditions will be explained in further detail in chapters 3.1.1 and 3.1.2.

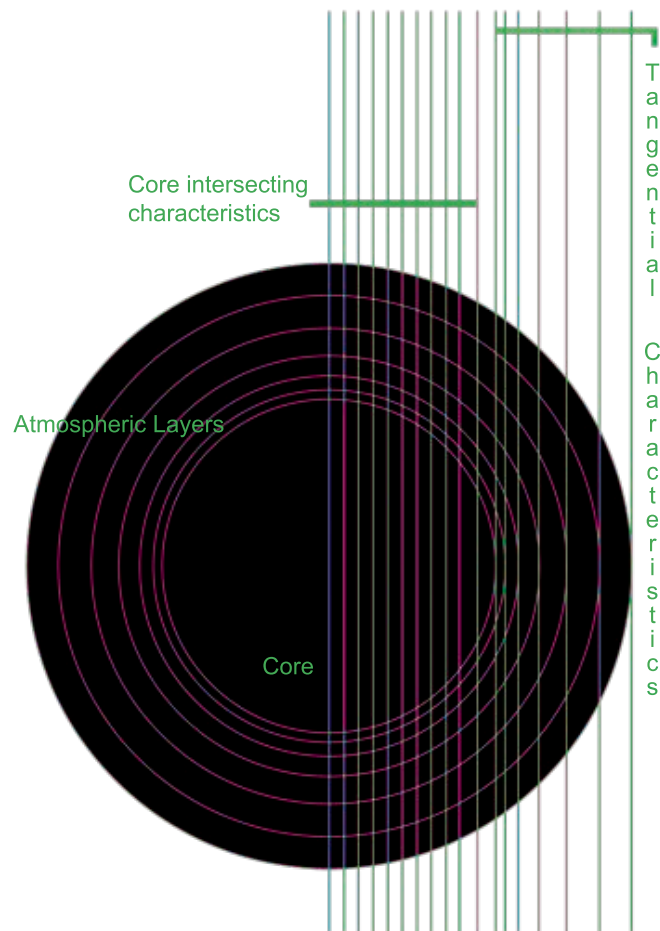


Figure 3.1: *Setup for the 1 dimensional spherical symmetric radiative transfer in PHOENIX.*

A PHOENIX 1D calculation follows the scheme as shown in figure 3.2. Either a starting atmosphere is read in from a previous calculation or the model starts from scratch with a gray atmosphere based on the given initial parameters, i.a.  $T_{\text{eff}}, \log_g, R_{\text{Planet}}, M_{\text{Planet}}$ . Within the gray atmosphere approximation the absorption coefficient does not depend on the wavelength. The initial opacity grid is calculated at a standard wavelength in between

the chosen maximum and minimum values, e.g.  $-10 \leq \log(\tau) \leq -4$ . The initial gray radiative equilibrium temperature stratification is build according to:

$$T(r) \approx T_{\text{eff}} \left( \frac{3}{4}\tau + \frac{1}{2} \right)^{1/4} \quad (3.1)$$

At low optical depths this means a nearly constant temperature. Using the structural information, the opacities are calculated computing each line profile individually at every radial point for each line within a search window of a few thousand Doppler widths. This way every line profile is calculated individually and every iteration anew. PHOENIX considers about 700 million molecular lines. The spectra that will be shown here are highly resolved and consist of over 470000 wavelength points. Within the wavelength loop, the radiative transfer is solved for each wavelength point until the full radiation field is known. At the end of each iteration the temperature correction (chapter 4.3) verifies the conservation of energy and de- or increases the temperature within the layers individually if needed. The next iteration then starts with the new corrected atmosphere structure. The temperature correction loop will be cycled until the model has converged.

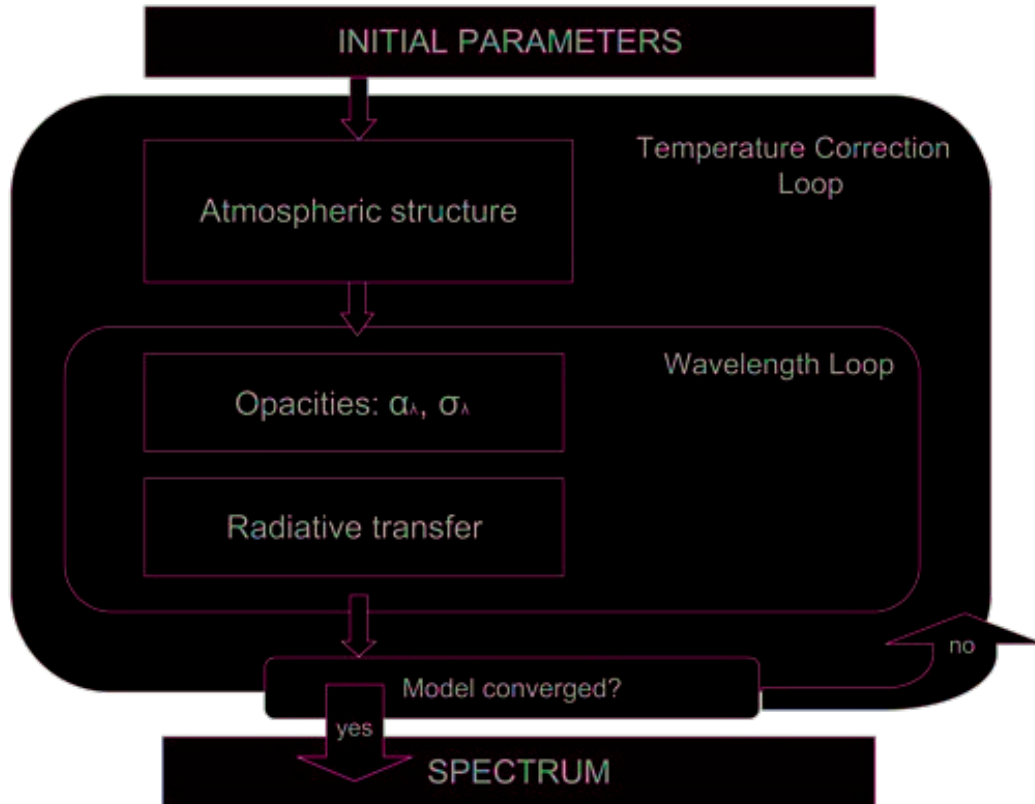


Figure 3.2: Flowchart for a general model calculation with PHOENIX 1D.

The geometrical setup of the 1D spherically symmetric model is shown in figure 3.1. The atmosphere is divided into a number of layers (here 64). All physical quantities are represented by their values in these layers. The radiative transfer is solved along the photon paths (described in chapter 4), also referred to as characteristics. The characteristic within the spherical 1D model can be differentiated into the tangential beams that just penetrate the atmosphere and the ones that hit the core. The treatment of these core intersecting characteristics is different for optically thin and thick exoplanets. In the optically thin regime reflection has to be taken into account.

The equation of radiative transfer can be solved introducing the  $\Lambda$ -operator. The theory of radiative transfer and the application of the operator splitting technique are outlined in chapter 4 and 4.1.

For the application on irradiated exoplanets, modifications to the main code, the formal solution, molecular array size and the accelerated lambda operator had to be implemented. Due to its improved equation of state (ACES), PHOENIX can calculate objects down to very low effective temperatures ( $T_{\text{eff}} \sim 250$  K). This temperature sets the lower limit for the calculation of cool objects with very low intrinsic temperatures. Earth's intrinsic temperature (i.e. taking no irradiation into account) is negligible and could be assumed  $T_{\text{int}} \sim 0$  K. At the moment this scenario is not recreatable. The lower temperature limit results from missing molecular and atomic data in that low temperature regime. Therefore for an Earth-twin, e.g., an intrinsic temperature of  $T_{\text{int}} = 280$  K will be used.

### 3.1.1 UPPER BOUNDARY CONDITION

The upper boundary condition of the secondary object (the exoplanet) is determined by the incident intensity impinging on the outermost atmospheric layer. Details on the conception and implementation of impinging radiation as the upper boundary condition can be found in Barman et al. (2001). The incident flux is given by:

$$F_{\nu}^{\text{inc}}(\tau_{\text{std}} = 0) = \left(\frac{R^{\star}}{d}\right)^2 F_{\nu}^{\star} \quad (3.2)$$

$R^{\star}$  is the radius of the primary,  $d$  the surface to surface distance of the primary to the secondary and  $F_{\nu}^{\star}$  is the monochromatic flux of the primary.  $F_{\nu}^{\star}$  is taken from a previously calculated (PHOENIX) input spectrum. The incident flux can be globally redistributed but here it is re-radiated by the dayside only. There are no restrictions in the choice of the host star.

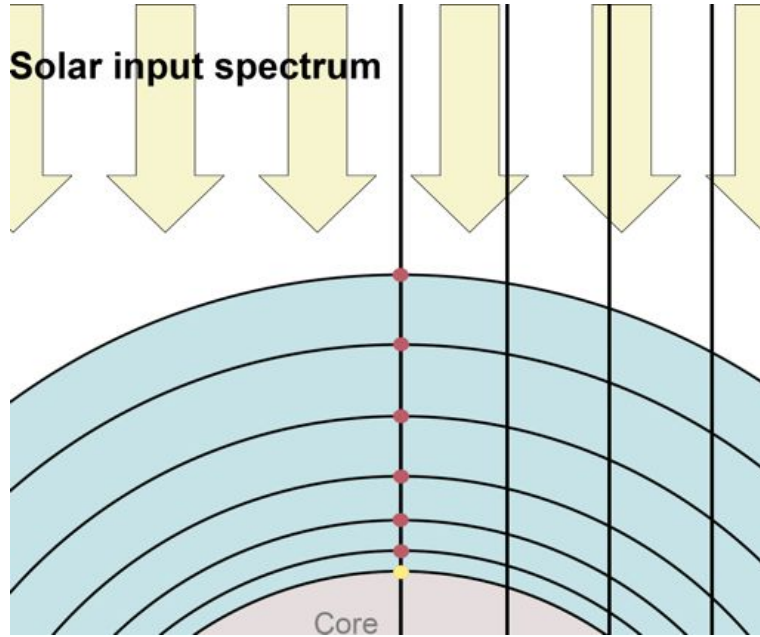


Figure 3.3: *The PHOENIX 1D irradiated planet model setup. The solar spectrum serves as the boundary condition at the uppermost atmospheric layer, the radiation transport is solved along a characteristic. For all layers local thermodynamic equilibrium (LTE) is assumed. The surface albedo is inserted at the lower boundary (yellow dot).*

### 3.1.2 LOWER BOUNDARY CONDITION / ALBEDO

The incident flux,  $F_{\text{inc}}$ , is partly reflected at the planetary surface and partly stored by the surface, resulting in a new effective temperature of the planet. The mathematical treatment of the lower boundary can be found in chapter 4.3.

#### ALBEDO

Since it is the primary goal of this thesis to simulate the influence of different surface types and thus different albedos on the reflectance spectrum, we need to declare what type of albedo is meant.

	<b>Bond</b>	<b>Geometric</b>		<b>Surface</b>	<b>Geometric</b>
Earth	0.306	0.376	⇒	Fresh snow	0.9
Venus	0.9	0.67		Old snow	0.45 - 0.9
Mars	0.25	0.17		Desert	0.3 - 0.4
Mercury	0.068	0.142		Forest	0.05 - 0.18
Jupiter	0.343	0.53		Ocean ice	0.5 - 0.7
Moon	0.11	0.12		Clouds	0.6 - 0.9
Saturn	0.342	0.47		Ocean	angular dependent

Table 3.1: *Left: different albedo values for solar system objects (Source: NASA planetary fact sheets) and for different surface types on the Earth (right).*

The term albedo (Latin for “whiteness”) is commonly used to describe the overall average diffuse reflectance of an object. The albedo determines the amount of light that is reflected by an object and thus the visual brightness of this object as well as the amount of energy that will be stored. It ranges in between  $0 \leq A \leq 1$ , with unity being a perfectly reflecting white surface (perfect mirror → no energy will be transferred to the surface) and zero being a perfect absorber (all energy will be stored, no reflection), see figure 3.4.

The geometric albedo of an astronomical body is the amount of radiation (at zero phase angle, i.e. along the direction of illumination) relative to that from a flat Lambertian (idealized flat, fully reflecting, diffusively scattering) surface which is an ideal reflector at

all wavelengths. Diffuse scattering implies that radiation is reflected isotropically. The spherical or Bond albedo (named after the American astronomer George Bond) is the total radiation reflected from an object (in all directions / all phase angles) compared to the total incident radiation from the Sun. Bond and geometrical albedos for some solar system objects are shown in table 3.1.2. The albedo I will further refer to is the Bond albedo. In order to model the effect of the surface albedo on a spectrum, the planetary atmosphere **must** be optically thin and ideally cloudless.

The surface types and thus albedos that are treated here are:

1. Constant, no wavelength dependence → gray
2. Angular dependent, Fresnel reflection → liquids
3. Wavelength dependent → Soil, vegetation, ice ..
4. Mixtures of 1-3

(1) In the case of a surface albedo  $A = 0$  all incoming energy is stored within the ground and heats up the surface. It is re-radiated as thermal (blackbody) radiation,  $F_{\text{inc}} + \sigma T_{\text{intr}}^4 = \sigma T_{\text{eff}}^4$ . In the other extreme case, the perfect mirror ( $A = 1$ ), all incoming radiation is reflected without any energy exchange with the surface:

$$F_{\text{inc}} + \sigma T_{\text{intr}}^4 = F_{\text{refl}} + \sigma T_{\text{intr}}^4 \quad (3.3)$$

Albedos of  $0 < A < 1$  represent shades of gray, see image 3.4. They just modify the amount of re-radiated light, not the shape of the incident spectrum in this wavelength range. The Earth has a wavelength averaged albedo (considering clouds) of  $A \sim 0.3$ .

(2) In the case of a water surface, for e.g. an ocean planet, the angular dependence of the reflectivity has to be taken into account. The light that hits the liquid surface with a  $90^\circ$  angle to the surface ( $\cos\theta = \mu = 0$ ) experiences the highest degree of absorption. With increasing  $\mu$  the amount of reflection rises. The effect is known from standing at the sea shore looking at the ocean. The water can appear silvery further out but is still blue and translucent close to the observer. This is known as the Fresnel effect and described by the Fresnel equations (equation 3.6). Fresnel reflection is directional and in a real environment, the albedo of a water surface is dominated by a diffuse reflection.

The values of the reflection and transmission coefficient depend on the polarization of the incident ray. The light polarized with the electric field of the light perpendicular to the plane of incidence (plane of the propagation direction and a vector perpendicular to

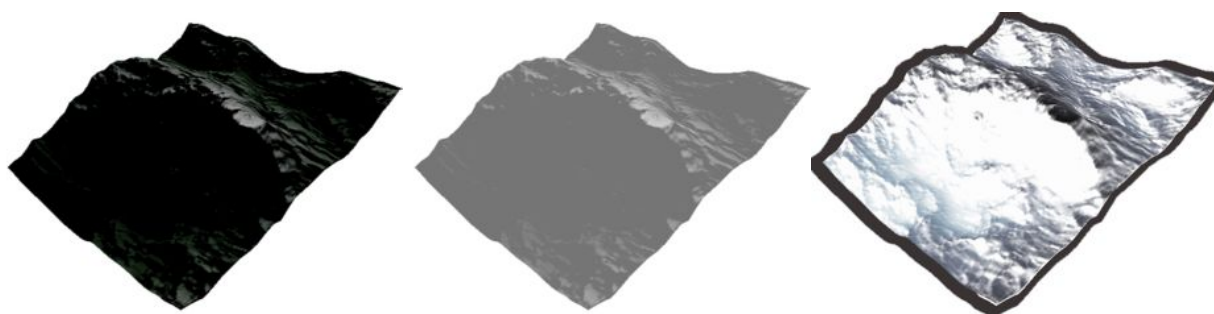


Figure 3.4: *The two extreme cases of surface “colors”. The perfect absorber (surface albedo is 0) and the perfect mirror (surface albedo is 1). The model outcome of perfectly absorbing surface basically produces a transmission spectrum, whereas a surface albedo  $> 0$  represent more-or-less-bright reflectance spectra.*

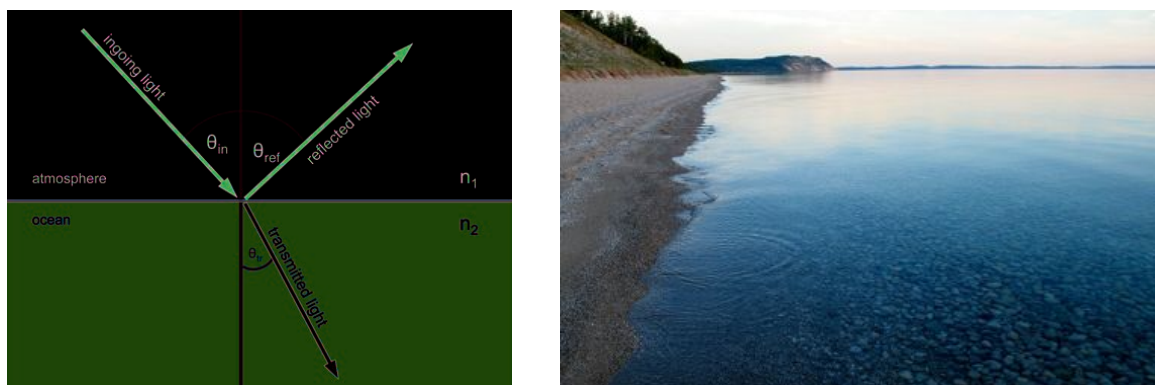


Figure 3.5: *The fresnel effect shown on a water surface. The absorption of light by water is highest (the reflection lowest) seen along the surface normal and decreases towards larger angles. Pictures taken from vacationideas.me.*

the plane of a reflecting surface) as shown in figure 3.5 is referred to as “S-polarized”. “P-polarized” light is polarized in the plane of the diagram. The designations “P” and “S” result from the german “senkrecht” and the english “parallel”. The angles of incident, reflected and transmitted light are related by  $\theta_{in} = \theta_{ref}$  and Snell’s law:

$$\frac{\sin(\theta_{in})}{\sin(\theta_r)} = \frac{n_{water}}{n_{air}} \quad (3.4)$$

with  $n_{air} \approx 1$  being the refractive index of air and  $n_{water}$  the refractive index of water  $\approx 1.3$ . When simulating other atmospheres and/or liquid surfaces (like e.g. a methane ocean), the refractive indexes have to be adjusted. The next equation describes the incoming and reflected beam(i), whereby (i) denotes a certain core intersecting characteristic.  $\mu$  is the

cosine of the impact angle taken from a matrix over all layers and angles:

$$\begin{aligned} \text{beam}_{\text{in}}(i) &= \pi - (\text{acos}(\mu_{\text{ray}}(\text{Layer}_{\text{surface}}, i))) \\ \text{beam}_{\text{out}}(i) &= \text{beam}_{\text{in}}(i)/n_{\text{water}} \end{aligned} \quad (3.5)$$

The Fresnel equations can then be written as:

$$\begin{aligned} S^{\text{pol}}(i) &= \left( \frac{\sin(\text{beam}_{\text{out}}(i)) - \sin(\text{beam}_{\text{in}}(i))}{\sin(\text{beam}_{\text{out}}(i)) + \sin(\text{beam}_{\text{in}}(i))} \right)^2 \\ P^{\text{pol}}(i) &= \left( \frac{\tan(\text{beam}_{\text{out}}(i)) - \tan(\text{beam}_{\text{in}}(i))}{\tan(\text{beam}_{\text{out}}(i)) + \tan(\text{beam}_{\text{in}}(i))} \right)^2 \end{aligned} \quad (3.6)$$

If the incident light is unpolarised, the reflection coefficient is:

$$A_{\text{water}(i)} = 0.5 \cdot (S^{\text{pol}}(i) + P^{\text{pol}}(i)) \quad (3.7)$$

Depending on the angle, the correct water albedo value is multiplied by the specific intensity at the lower boundary. The quantity  $A_{\text{water}} = \frac{1}{n} \sum_{i=0}^n A_{\text{water}(i)}$  is an important average needed within the temperature correction.

The ocean surface albedo does not vary with the angle alone, it is also sensitive to the wind speed, ocean chlorophyll concentration and aerosol/cloud optical depth. But these dependences will be neglected here.

(3) All real surfaces have a wavelength dependent reflectance.



Figure 3.6: *Different possible worlds. Deserted and snow worlds can also exist outside of the habitable zone. The picture in the middle shows an inhabited world with a moist atmosphere.*

## SNOW &amp; ICE

The reflectance of snow and ice is a measure of the grain size, solar zenith angle, snow layer thickness, ratio of diffuse to direct incident flux. The snow reflectance is furthermore influenced by the amount of water within the snow flakes. The ice reflectance depends on the bubble content. With increasing grain size and water content the reflectance decreases. Thus fresh snow has a higher reflectance than older, clumpier snow. The albedo increases with increasing zenith angle at all wavelengths. The albedo of snow is high in the near-UV and the visible and decreases steeply in the near-IR and stays low towards larger wavelengths. Wiscombe & Warren (1980) calculated the snow albedo considering all the above mentioned factors and compared the results to the measurements of O'Brian and Munis (1975), who measured the snow reflectance in the laboratory.

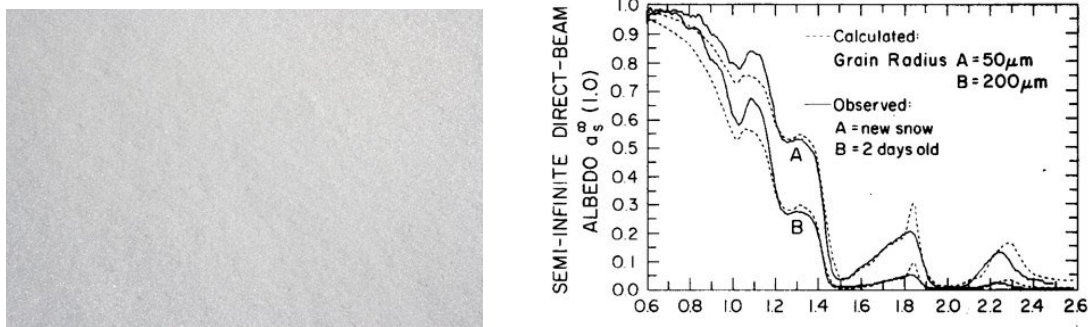


Figure 3.7: *The reflectivity of snow is highest for fresh snow. Right: Measured reflectivity curves for fresh and older snow, found in Wiscombe & Warren (1980).*

The reflectance curve used for the simulation in chapter 5.7 is the one shown in figure 3.7 by Wiscombe & Warren (1980).

## SAND & DESERT

The composition of sand or regolith<sup>2</sup> is variable. However, the major components are silicon dioxide  $\text{SiO}_2$ , alumina  $\text{Al}_2\text{O}_3$ , iron oxide  $\text{FeO}$ , calcium oxide  $\text{CaO}$  and magnesium oxide  $\text{MgO}$ . The geologist J.N. Rinker measured reflectance curves of a variety of soils. The samples were taken from sand dunes, areas around volcanos, granites and gravel for the U.S. Army Topographic Engineering Center. The reflectance was measured in between 400 and 2400 nm. Comparing the samples of sands from different locations they all share a common shape with a dip in reflectance around 400 nm and bumpy plateau in between 700 to 2400 nm. Mixtures dominated by granite or of volcanic origin are lower in reflectance and have, in general, no outstanding features in their albedo curves. Evans et al. (1982) found a good sample match for the comparison to martial samples in weathered basalts of semi-arid areas on Hawaii. Those basalts were oxidized by weathering or volcanic activity and thus Evans et al. (1982) suggested that this congruities with the Hawaiian samples might be an evidence that similar processes occurred in the past on Mars.

For the martian planet (chapter 5.8) I used the albedo curve shown in picture 3.8 on the right-hand side.

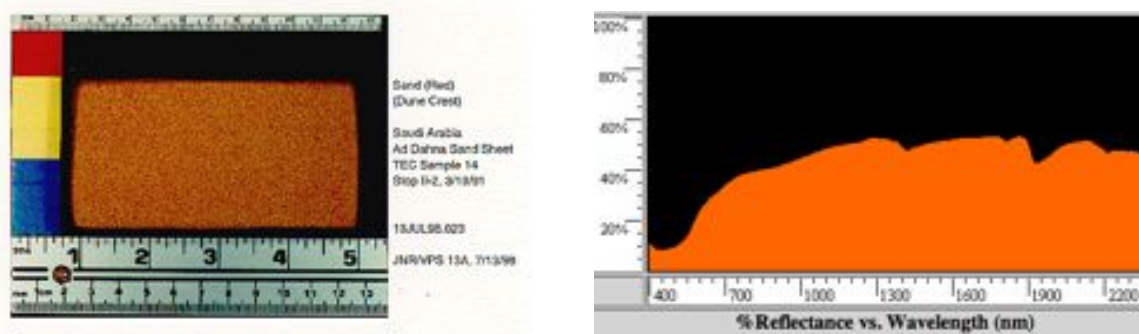


Figure 3.8: *The wavelength dependent albedo measured from a sample of a dune crest in Saudi Arabia. Picture source: [www.agc.army.mil/research/products/desert\\_guide/lspectra/lspec1.htm](http://www.agc.army.mil/research/products/desert_guide/lspectra/lspec1.htm)*

<sup>2</sup>a surface layer of loose, heterogeneous material

## VEGETATION

The vegetation red edge has been introduced earlier in chapter 2.2. This is the ultimate sign of vegetation as we know it from the combination Earth-Sun. The graph in figure 2.5 displays the VRE data that was used for the simulation in chapter 5.9.

On other planets that are orbiting other stars, photosynthetic organisms might be of other color, adapting to the spectrum of light that reached them. Photosynthesis could be powered by any kind of light in the visible spectrum. Plants on planets around cooler stars like M dwarfs would probably try to catch any light they could get, resulting in a darker leaf color. Around hotter stars, plants would absorb more of the blue light and could appear yellow or red.

Minerals like sulfur, cinnabar or hematite show sharp rises in their reflectivity around the same wavelengths like the VRE (figure 3.9). So there is a risk of a false detection of life.

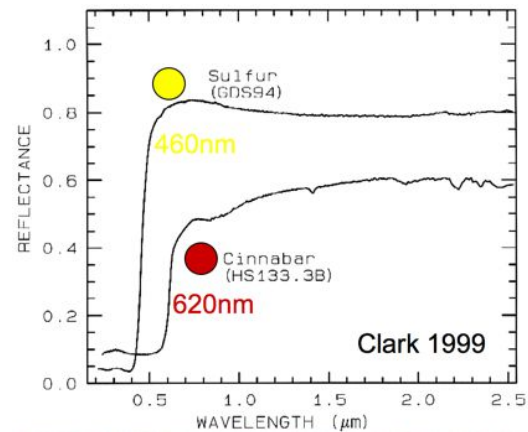
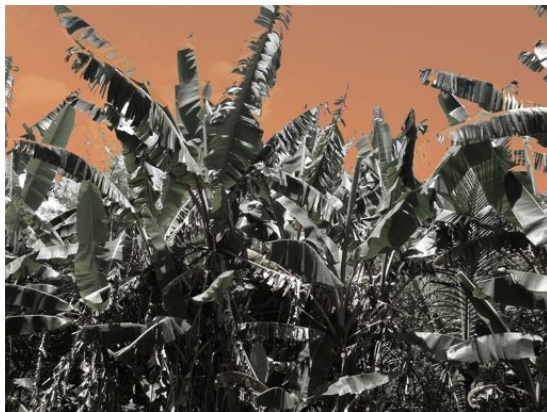


Figure 3.9: *Left: Photosynthesis plants on planets that are orbiting red dwarf might be of black color in the intention of catching every light they can get. Right: Minerals can mimic the VRE.*

---

# Chapter 4

## RADIATIVE TRANSFER

This chapter introduces the quantities of the theory of radiative transfer that are important to this work. For more details on the theory of radiative transfer I refer to the well known work of Chandrasekhar (1960), Rutten (2003) or Mihalas (1978).

### 1D MOMENTS OF THE RADIATION FIELD

The specific intensity is the amount of energy emitted in a solid angle from a point  $\mathbf{r}$  from a surface element at time  $t$  in direction  $\mathbf{n}$  per second and per wavelength:

$$I_\nu = \frac{dE_\nu}{(d\sigma \cos\theta) d\omega d\nu dt}, \quad \left[ \frac{\text{erg}}{\text{cm}^2 \cdot \text{s} \cdot \text{Hz} \cdot \text{sr}} \right]_{\text{cgs}} \quad (4.1)$$

Integrating equation 4.1 over all solid angles provides the moments of the radiation field. The zeroth moment corresponds to the mean intensity  $J_\nu$ :

$$J_\nu = \frac{1}{2} \int_{-1}^{+1} I_\nu d\mu \quad (4.2)$$

with  $\mu = \cos\theta$ ,  $J_\nu = I_\nu$  for an isotropic radiation field. The first moment of the radiation field is the Eddington flux:

$$H_\nu = \frac{1}{2} \int_{-1}^{+1} I_\nu \mu d\mu \quad (4.3)$$

The second moment is called the K-integral:

$$K_\nu = \frac{1}{2} \int_{-1}^{+1} I_\nu \mu^2 d\mu \quad (4.4)$$

**MOMENTS OF THE RADIATIVE TRANSFER EQUATION**

The equation of radiative transfer in the steady state, 1D spherically symmetric case can be written as (Mihalas (1978), p.33):

$$\mu \frac{\partial I_\nu}{\partial r} + \frac{1 - \mu^2}{r} \frac{\partial I_\nu}{\partial \mu} = (\kappa_\nu + \sigma_\nu) \cdot (S_\nu - I_\nu) \quad (4.5)$$

with  $\kappa_\nu$  the absorption and  $\sigma_\nu$  the scattering coefficient,  $\mu = \cos\theta$ , with  $\theta$  as the angle between the vector normal to the surface and  $I_\nu$ , the specific intensity. The source function is defined as the ratio of emissivity,  $j_\nu$ , to extinction,  $\chi_\nu = \kappa_\nu + \sigma_\nu$ , with  $\kappa_\nu$  the absorption- and  $\sigma_\nu$  the scattering coefficient,

$$S_\nu \equiv \frac{j_\nu}{\kappa_\nu + \sigma_\nu} = \frac{j_\nu}{\chi_\nu} \quad (4.6)$$

In thermodynamic equilibrium,  $I_\nu = B_\nu$  and  $I = \int_0^\infty I_\nu d\nu = B(T)$  where  $B_\nu(T)$  is the Planck function. The absorption, scattering and emission are caused by atomic and molecular bound-bound, bound-free and free-free transitions. The optical depth  $\tau_\nu$  is a measure of transparency of the matter. It is increasing from the outermost atmospheric shell towards the object's surface, which explains the negative sign in equation (4.7):

$$d\tau_\nu := -\rho\chi_\nu dz \quad (4.7)$$

Along a characteristic the monochromatic formal solution for the inward (-) and outward (+) going radiation can be written as:

$$I^-(\tau_i, \mu, \nu) \equiv I^-(\tau_{i-1}, \mu, \nu) \cdot e^{-\Delta\tau_{i-1}} + \Delta I_i^-(S, \mu, \nu) \quad (4.8a)$$

$$I^+(\tau_i, \mu, \nu) \equiv I^+(\tau_{i+1}, \mu, \nu) \cdot e^{-\Delta\tau_i} + \Delta I_i^+(S, \mu, \nu) \quad (4.8b)$$

$\tau_1$  is zero at the outermost atmospheric layer and increases towards the surface  $\tau_{i-1} \leq \tau_i$ .  $\Delta\tau_i$  then is derived by, e.g., linear interpolation along the ray  $\Delta\tau_{i-1} = (\tau_{i-1} + \tau_i) / |\mu|$ .

The change in the specific intensity from layer  $i - 1$  to layer  $i$  can be constructed from a linear or parabolic polynomial interpolation of the source function:

$$\Delta I_i^\pm = \alpha_i^\pm S_{i-1} + \beta_i^\pm S_i + \gamma_i^\pm S_{i+1} \quad (4.9)$$

---

with the parabolic coefficients (Olson & Kunasz (1987)):

$$\alpha_i^- = \frac{e_{0i} + e_{2i} - (\Delta\tau_i + 2\Delta\tau_{i-1})e_{1i}}{\Delta\tau_{i-1}(\Delta\tau_i + \Delta\tau_{i-1})} \quad (4.10a)$$

$$\beta_i^- = \frac{(\Delta\tau_i + \Delta\tau_{i-1})e_{1i} - e_{2i}}{\Delta\tau_{i-1}\Delta\tau_i} \quad (4.10b)$$

$$\gamma_i^- = \frac{e_{2i} - \Delta\tau_{i-1}e_{1i}}{\Delta\tau_i(\Delta\tau_i + \Delta\tau_{i-1})} \quad (4.10c)$$

$$\alpha_i^+ = \frac{e_{2i+1} - \Delta\tau_{i-1}e_{1i+1}}{\Delta\tau_{i-1}(\Delta\tau_i + \Delta\tau_{i-1})} \quad (4.10d)$$

$$\beta_i^+ = \frac{(\Delta\tau_i + \Delta\tau_{i-1})e_{1i+1} - e_{2i+1}}{\Delta\tau_{i-1}\Delta\tau_i} \quad (4.10e)$$

$$\gamma_i^+ = \frac{e_{0i+1} + e_{2i+1} - (\Delta\tau_{i-1} + 2\Delta\tau_i)e_{1i+1}}{\Delta\tau_i(\Delta\tau_i + \Delta\tau_{i-1})} \quad (4.10f)$$

and in the linear case:

$$\alpha_i^- = \frac{e_{0i} - e_{1i}}{\Delta\tau_{i-1}} \quad (4.11a)$$

$$\beta_i^- = \frac{e_{1i}}{\Delta\tau_{i-1}} \quad (4.11b)$$

$$\gamma_i^- = 0 \quad (4.11c)$$

$$\alpha_i^+ = 0 \quad (4.11d)$$

$$\beta_i^+ = \frac{e_{1i+1}}{\Delta\tau_i} \quad (4.11e)$$

$$\gamma_i^+ = \frac{e_{0i+1} - e_{1i+1}}{\Delta\tau_i} \quad (4.11f)$$

$e_{0i}$ ,  $e_{1i}$  and  $e_{2i}$  are auxiliary functions:

$$e_{0i} = 1 - \exp(-\Delta\tau_{i-1}) \quad (4.12a)$$

$$e_{1i} = \Delta\tau_{i-1} - e_{0i} \quad (4.12b)$$

$$e_{2i} = (\Delta\tau_{i-1})^2 - 2e_{1i} \quad (4.12c)$$

These coefficients  $\alpha_i^\pm, \beta_i^\pm$  and  $\gamma_i^\pm$  (equation 4.9 - 4.12) are used to construct the  $\Lambda^*$ -operator.

---

## 4.1 OPERATOR SPLITTING METHOD

In the spherically symmetric 1D case, the characteristics are treated differently depending on whether they intersect the core or not (figure 3.1). First, I will give a short introduction into the operator splitting method as it is used in PHOENIX (further details can be found e.g. in Hauschildt et al. (1994)). Then I will show how core-intersecting characteristics must be treated with a reflective lower boundary.

PHOENIX uses the method the operator splitting method. In the case of radiative transfer problems the eigenvalues of the conventional  $\Lambda$ -operator are known to be close to unity and thus the convergence rate is poor. To save computing time, the approximate lambda operator (ALO) is introduced. This operator should possess two properties: the physical properties of the normal  $\Lambda$ -operator to generate  $J_\nu$  from  $S_\nu$  and it should be save computing time (through fast convergence). With  $n$  denoting the current iteration and  $n+1$  the upcoming iteration step, the conventional  $\Lambda$ -operator can be split:

$$\Lambda = \Lambda^* + (\Lambda - \Lambda^*) \tag{4.13}$$

The mean intensity is then given by:

$$J^{n+1} = \Lambda^* S^{n+1} + (\Lambda - \Lambda^*) S^n \tag{4.14}$$

To derive the new Source function, the new mean intensity is calculated with the  $J^n$  of the current iteration and  $J^{FS} = \Lambda S^n$ :

$$[1 - \Lambda^*(1 - \epsilon)] J^{n+1} = J^{FS} - \Lambda^*(1 - \epsilon) J^n \tag{4.15}$$

In the case of thermal equilibrium and without scattering,  $S_\nu = B_\nu = I_\nu$  and the radiative transfer equation can be solved analytically according to equation 4.8. More information on the construction of the  $\Lambda^*$ -operator for arbitrary bandwidth can be found in Hauschildt et al. (1994).

## 4.2 MODIFICATIONS TO THE $\Lambda^*$ -OPERATOR

In the following section the construction of the  $\Lambda^*$  for a single characteristic will be explained, both for the optically thick and the optically thin case including reflection.

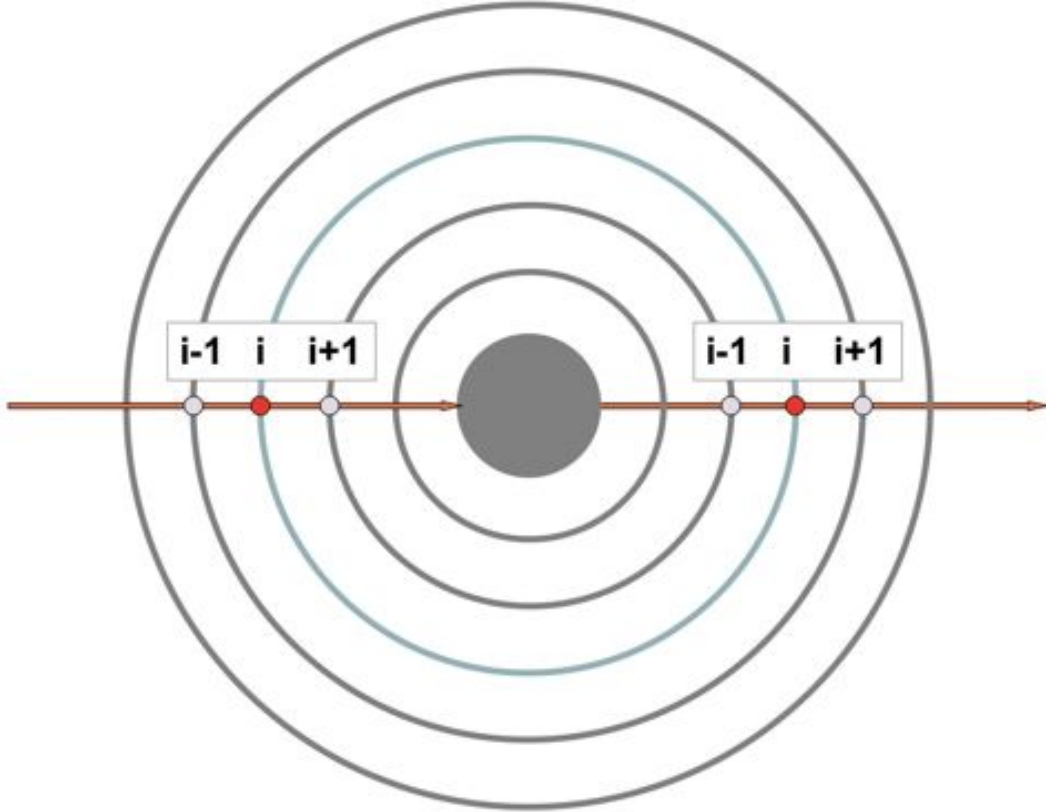


Figure 4.1: *The construction scheme for the  $\Lambda^*$ -operator.*

The layer in which  $S$  is set to unity will have the index  $i$ , the previous layer  $i - 1$  and the following layer  $i + 1$ , as shown in figure 4.1. The outermost atmospheric layer ( $i = 1$  for ingoing,  $i = 64$  for outgoing characteristics) and the innermost layer ( $i = 64$  for ingoing and  $i = 1$  for outgoing characteristics) have to be constructed separately. The  $\Lambda^*$ -operator for all layers in between can be built within one loop.

Table 4.1 shows the construction of the contributions to the specific intensity according to equations 4.8 and 4.9 exemplarily for a single ingoing characteristic. They will be denoted as  $s_1^-$ ,  $s_2^-$  and  $s_3^-$  ( $s_1^-$  for the previous,  $s_2^-$  the actual and  $s_3^-$  the next layer. Integrated over frequency and angle they will be needed later to construct the  $\Lambda$ -matrix. It should

be noted that the diffusion approximation holds at the inner boundary in case of optically thick planetary atmospheres and the  $\Lambda_{\text{planet}}^*$  reduces to the the  $\Lambda_{\text{star}}^*$ . All parameters described in the tables 4.1 and 4.2 are arrays of the layer  $i$  and the solid angles:

	$\Lambda_{\text{star}}^*$	$\Lambda_{\text{planet}}^*$
$i = 1 :$	$s_2^- = \beta_1^-$ $s_3^- = s_2^- \cdot e^{-\Delta\tau_1} + \alpha_2^-$	$s_2^- = \beta_1^-$ $s_3^- = s_2^- \cdot e^{-\Delta\tau_1} + \alpha_2^-$
$i = 64 :$	$s_1^- = \gamma_{63}^-$ $s_2^- = s_1^- \cdot e^{-\Delta\tau_{63}} + \beta_{64}^-$	$s_1^- = \gamma_{63}^-$ $s_{2\text{in}}^- = s_1^- \cdot e^{-\Delta\tau_{63}} + \beta_{64}^-$ <p style="text-align: center; color: orange;">saved for reflection</p>
$i = 2, 63 :$	$s_1^- = \gamma_{i-1}^-$ $s_2^- = s_1^- \cdot e^{-\Delta\tau_{i-1}} + \beta_i^-$ $s_3^- = s_2^- \cdot e^{-\Delta\tau_i} + \alpha_{i+1}^-$	$s_1^- = \gamma_{i-1}^-$ $s_2^- = s_1^- \cdot e^{-\Delta\tau_{i-1}} + \beta_i^-$ $s_3^- = s_2^- \cdot e^{-\Delta\tau_i} + \alpha_{i+1}^-$

Table 4.1: Construction of the  $s_1^-, s_2^-, s_3^-$  for the ingoing characteristics.

Table 4.1 shows that the inward construction of the planetary  $\Lambda^*$ -elements corresponds to the stellar case, just the reflection at the planetary surface requires  $s_{2\text{in}}^-$  to be saved. The upper and the lower boundary are treated separately because they are both lacking either the previous or the following layer.

The tricky part is the construction of the outgoing characteristics (table 4.2). Note that the indices change now! They are running from the innermost layer which is now layer 1 ( $i = 1$ ) to the outermost layer  $i = 64$ , by analogy to the way it is done in PHOENIX. The reflective boundary requires the consideration of two major changes within the construction of the  $\Lambda^*$ -operator:

1.  $s_{2\text{in}}$  becomes part of  $s_{2\text{out}}$
2. “Pulse tracking”

(1) As in the case of the outermost layer, there is no layer previous to the surface. At the inner boundary,  $s_{2\text{in}}$  is picked up within the expression for  $s_{2\text{out}}$  and multiplied to the surface albedo plus the contribution of the surface layer in the form of  $\beta_1$ . The  $s_3$ -term needs to be saved and passed on to the  $s_1$ -term of the next layer. This basically means that the intensity input of the reflection is contributing to the intensity in every following layer. (2) In a sense this process tracks the remnant of the “pulse” that was added by the reflection throughout the atmosphere.

$\Lambda_{\text{star}}^*$	$\Lambda_{\text{planet}}^*$
$i = 1 :$	
$s_2^+ = \beta_1^+$	$s_{2\text{out}}^+ = \beta_1^+ + s_{2\text{in}}^- \cdot A_{\text{surface}}$
$s_3^+ = s_2^+ \cdot e^{-\Delta\tau_1} + \alpha_2^+$	$s_3^+ = s_2^+ \cdot e^{-\Delta\tau_1} + \alpha_2^+$
	$s_3^+ \text{save} = s_3^+ \text{ saved for tracking}$
$i = 64 :$	
$s_1^+ = \gamma_{63}$	$s_1^+ = s_3^+ \text{save} \cdot e^{-\Delta\tau_{62}} + \gamma_{63}^+$
$s_2^+ = s_1^+ \cdot e^{-\Delta\tau_{63}} + \beta_{64}^+$	$s_2^+ = s_1^+ \cdot e^{-\Delta\tau_{63}} + \beta_{64}^+$
$i = 2, 63 :$	
$s_1^+ = \gamma_{i-1}^+$	for $i - 2 > 0$ :
	$s_1^+ = s_3^+ \text{save} \cdot e^{-\Delta\tau_{i-2}} \cdot A_{\text{surface}}$
	for $i - 2 = 0$ :
	$s_1^+ = s_3^+ \text{save}$
$s_2^+ = s_1^+ \cdot e^{-\Delta\tau_{i-1}} + \beta_i^+$	$s_2^+ = s_1^+ \cdot e^{-\Delta\tau_{i-1}} + \beta_i^+$
$s_3^+ = s_2^+ \cdot e^{-\Delta\tau_i} + \alpha_{i+1}^+$	$s_3^+ = s_2^+ \cdot e^{-\Delta\tau_i} + \alpha_{i+1}^+$

Table 4.2: Construction of  $s_1^+, s_2^+, s_3^+$  for the outgoing characteristics.

Now it is possible to calculate the elements of the matrix below, on and above the main diagonal are  $A_i$ ,  $B_i$  and  $C_i$ :

$$A_{i+1} = \int_{-\infty}^{+\infty} \phi_\nu d\nu \int_0^1 \frac{1}{2} (s3_{i+i}^- + s3_{i+i}^+) \quad (4.16a)$$

$$B_i = \int_{-\infty}^{+\infty} \phi_\nu d\nu \int_0^1 \frac{1}{2} (s3_i^- + s3_i^+) \quad (4.16b)$$

$$C_{i-1} = \int_{-\infty}^{+\infty} \phi_\nu d\nu \int_0^1 \frac{1}{2} (s3_{i-1}^- + s3_{i-1}^+) \quad (4.16c)$$

The implementation can be tested by sending a pulse through every layer for a single wavelength. The  $\Lambda^*$ -operator is successfully constructed when:

$$\Lambda_{i+1,j}^* = J_{i+1} = A_{i+1} \quad (4.17a)$$

$$\Lambda_{i,j}^* = J_i = B_i \quad (4.17b)$$

$$\Lambda_{i-1,j}^* = J_{i-1} = C_{i-1} \quad (4.17c)$$

Although for a first test it is recommended to compare the outgoing specific intensities with the  $s_1^+$ ,  $s_2^+$ ,  $s_3^+$  for a single characteristic and a single wavelength. The comparison follows the same scheme as used in equations 4.17.

### 4.3 TEMPERATURE CORRECTION

The temperature correction at the end of each iteration guarantees the conservation of energy. PHOENIX 1D uses the Unsöld-Lucy (UL) method to add a correction term to the gas temperature to each layer at the end of each iteration. This method was introduced by Unsöld for the gray atmosphere and extended by Lucy for non-gray atmospheres. The Unsöld-Lucy procedure is based on the fact, that the ratios of the absorption means (Planck mean  $\kappa_P$ , absorption mean  $\kappa_J$  and flux mean  $\kappa_H$ ) do not change much from one iterative step to the next.

First I will briefly outline the UL-method which is valid for very atmospheric layer except for the planetary surface layer (in the optically thin case) and then explain the modifications at the top and last layer. Further information on the UL-method can be found in e.g. Lucy (1964) or Hauschildt et al. (2003).

The moments of the radiative transfer equation can be derived by applying the operators  $\frac{1}{2} \int_{-1}^1 d\mu$  and  $\frac{1}{2} \int_{-1}^1 \mu d\mu$  to equation 4.5:

$$-(\kappa_\nu + \sigma_\nu)\rho H_\nu = \frac{\partial}{\partial r} K_\nu + \frac{3K_\nu - J_\nu}{r} \quad (0. \text{ moment}) \quad (4.18a)$$

$$\frac{\partial}{\partial r} r^2 H_\nu = -(\kappa_\nu + \sigma_\nu)\rho r^2 (J_\nu - S_\nu) \quad (1. \text{ moment}) \quad (4.18b)$$

The mean opacities are defined as:

$$\kappa_P = \frac{1}{B} \int_0^\infty \kappa_\nu B_\nu d\nu \quad (4.19a)$$

$$\kappa_J = \frac{1}{J} \int_0^\infty \kappa_\nu J_\nu d\nu \quad (4.19b)$$

$$\kappa_H = \frac{1}{H} \int_0^\infty (\kappa_\nu + \sigma_\nu) H_\nu d\nu \quad (4.19c)$$

Integrating equations 4.18a and 4.18b over frequency, the mean opacities can be inserted which leads to an expression for the radiative transfer moments equations as so:

$$-\rho \kappa_H H = \frac{\partial}{\partial r} K + \frac{3K - J}{r} \quad (4.20a)$$

$$\frac{\partial}{\partial r} r^2 H = \rho \kappa_P r^2 (\kappa_J / \kappa_P \cdot J - B) \quad (4.20b)$$

Using an approximate expression for the source function  $S_\nu = (\kappa_\nu B_\nu + \sigma_\nu J_\nu) / (\kappa_\nu + \sigma_\nu)$  and introducing the variable Eddington factor  $f = \frac{K}{J}$  and a sphericity function  $q$ ,

the moments equations are now solely functions of the optical depth. It is now taken advantage of the fact that the ratios of the means do not differ much from the actual to the next iteration  $\frac{\kappa_H}{\kappa_P} = \frac{\kappa'_H}{\kappa'_P}$  and  $\frac{\kappa_J}{\kappa_P} = \frac{\kappa'_J}{\kappa'_P}$  and the same is assumed for the Eddington factor  $f' = f$ . That yields:

$$\frac{\partial}{\partial \tau}(qf\Delta J) = q\frac{\kappa_H}{\kappa_P}\Delta H \quad (4.21a)$$

$$\frac{\partial}{\partial \tau}(\Delta H) = \left(\frac{\kappa_J}{\kappa_P}\Delta J + \Delta B\right) \quad (4.21b)$$

with  $\Delta J = J - J'$  and  $\Delta H = H - H_{\text{target}}$ . Solving 4.21a for  $\Delta J$  and inserting that into equation 4.21b, gives a first expression for the correction term we are searching for. Note that  $\frac{d\Delta H}{d\tau} = \frac{\kappa_J}{\kappa_P}J - B$  and by using the (second) Eddington approximation  $J(0) = 2H(0)$ , this leads to the expressions:

$$\Delta B = \Delta B_1 + \Delta B_2 \quad \text{with} \quad (4.22a)$$

$$\Delta B_1 = \frac{\kappa_J}{\kappa_P}J - B \quad \text{and} \quad (4.22b)$$

$$\Delta B_2 = \frac{\kappa_J}{\kappa_P} \left( 2q(0)f(0)\Delta H(0) + \int_0^\tau q\frac{\kappa_H}{\kappa_P}\Delta H d\tau' \right) \frac{1}{qf} \quad (4.22c)$$

Equation 4.22b treats the optical thin part of the atmosphere (or in the case of the planetary model the whole atmosphere), since this term becomes small at high pressures, densities and opacities ( $S \rightarrow B$ ). In the optical thick regime equation 4.22c contributes the crucial correction.

The correction term for the gas temperature is finally obtained using the Stefan-Boltzmann law:

$$\Delta T = \frac{\Delta B}{4\sigma T^3 r^2} \quad (4.23)$$

### IN CASE OF IRRADIATION

The temperature correction scheme described above does not account for irradiation. To do that, the target flux  $H_{\text{target}}$  has to be replaced by the expression  $H_{\text{target}} = H_{\text{ext}} + \sigma T_{\text{intr}}^4$ . The target flux now consists of the intrinsic part that is contributed by the planet's intrinsic temperature,  $\sigma T_{\text{intr}}^4$ , and the incident (extern) Eddington flux,  $H_{\text{ext}}$ , of the host star. If the planets own contribution to the total flux is much lower than the incident flux the following important modification has to be made in equation 4.22 (Barman et al. (2001)).

$$\Delta B = \Delta B_1 + \Delta B_2 \quad \text{with} \quad (4.24a)$$

$$\Delta B_1 = \frac{\kappa_{\text{J}}^{\text{int}}}{\kappa_{\text{P}}} J_{\text{int}} - B \quad \text{and} \quad (4.24b)$$

$$\Delta B_2 = \frac{\kappa_{\text{J}}^{\text{int}}}{\kappa_{\text{P}}} \left( 2q(0)f_{\text{int}}(0)\Delta H^{\text{int}}(0) + \int_0^\tau q \frac{\kappa_{\text{H}}^{\text{int}}}{\kappa_{\text{P}}} (H_{\text{int}} - H_{\text{target}} \cdot \kappa_{\text{H}}^{\text{int}}) d\tau' \right) \frac{1}{qf_{\text{int}}} \quad (4.24c)$$

The incident radiation can be assumed to be constant, so most of the quantities will be dependent on the intrinsic part only. But since the flux has a direction and it is set to  $H_{\text{int}} > 0$  and  $H_{\text{ext}} < 0$ , negative total fluxes  $H_{\text{total}} = H_{\text{int}} + H_{\text{ext}}$  can occur. This is the case when modeling Earth-like rocky planets that have a very low intrinsic temperature or in general when the incoming flux exceeds the intrinsic flux. The flux of a possibly habitable exoplanet will peak in different regions than the flux of its host star, resulting in a negative  $\kappa_{\text{H}}$ . Without the modification of  $\kappa_{\text{H}}$  to  $\kappa_{\text{H}}^{\text{int}}$  in the integrand of equation 4.24c, the temperature would be corrected in the wrong direction.

## 4.4 MODIFICATIONS TO THE TEMPERATURE CORRECTION

Due to the surface albedo, a fraction of the incident light is stored within the ground and increases the effective temperature of the planet. The approximation used in the planetary

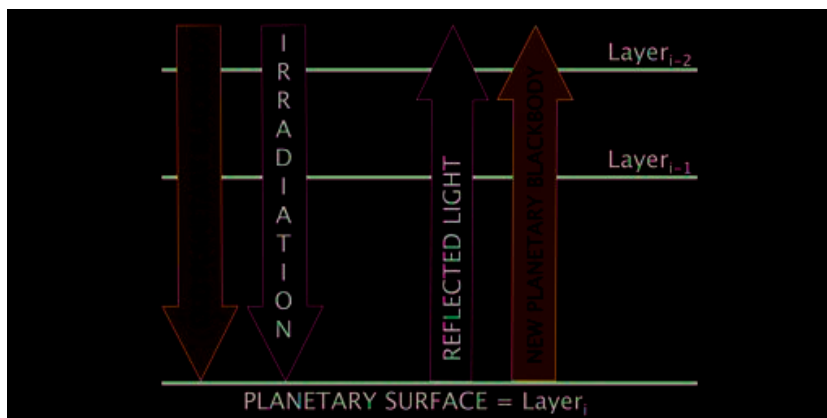


Figure 4.2: *The net flux in the planetary model is zero. The incoming equals the outgoing flux.*

model takes advantage of the constant energy input by the host star and the optically thin atmosphere. The incoming flux is not significantly altered by the atmosphere until it reaches the surface.

Equation 4.25a and 4.25b correspond to the yellow arrows in figure 4.2:

$$F_{\text{irrad}}^{\text{in}} = L / (16 \cdot \pi \cdot R_{\text{Planet}}^2) \quad (4.25a)$$

$$F_{\text{irrad}}^{\text{out}} = F_{\text{irrad}}^{\text{in}} \cdot A_{\text{gray}} \quad (4.25b)$$

$$F_{\text{irrad}}^{\text{save}} = (1 - A_{\text{gray}}) \cdot F_{\text{irrad}}^{\text{in}} \quad (4.25c)$$

For the wavelength dependent albedo, the  $A_{\text{gray}}$  is replaced by the wavelength averaged albedo  $\bar{A}_{\text{color}}$ , for water albedo it is  $\bar{A}_{\text{water}}$ . There is a net flux of zero in all layers since all the incoming flux must equal the emitted flux in this model. The left side of equation 4.26 describes the incoming, the right side describes the outgoing part.

$$\sigma T_{\text{intrinsic}}^4 + F_{\text{irrad}}^{\text{in}} = F_{\text{irrad}}^{\text{out}} + \sigma T_{\text{surf}}^4 \quad (4.26)$$

In the first iteration the original effective temperature without irradiation (or intrinsic temperature) is replaced by the new surface temperature  $T_{\text{surf}}$  under consideration of the incoming irradiation.

$$T_{\text{surf}} = \left( \frac{\sigma \cdot T_{\text{orig}}^4 + F_{\text{irrad}}^{\text{save}}}{\sigma} \right)^{1/4} \quad (4.27)$$

The new surface temperature is now used as the new effective temperature for all follow-up routines within the code and all following iterations. From iteration 2 until the last iteration, the temperature within the layers is corrected by the Unsöld-Lucy (UL) method according to equation 4.24.

# Chapter 5

## RESULTS

In this chapter I will discuss the results of my simulations. They span the solar system planets Earth, Venus and a Mars-like object, the super-Earth GJ1214 b and the hypothetical Gliese 581g. Furthermore the Earth in two past evolutionary stages and models of an snowball planet, an ocean world and a world that is completely covered by plants. A list of the molecular bands that I used to interpret the spectra is provided in table 5.1.

### Absorption bands [ $\mu\text{m}$ ]

CO <sub>2</sub>	1.21, 1.4, 1.57, 1.6, 2.0, 2.7, 4.3, 4.8, 5.2, 15
H <sub>2</sub> O	0.51, 0.57, 0.61, 0.65, 0.72, 0.82, 0.94, 1.1, 1.13, 1.38, 1.41, 1.87, 2.7, 3.2, 6.3, 12 - microwave
O <sub>2</sub>	0.58, 0.69, 0.76, 1.27
O <sub>3</sub>	0.45-0.75, 9.6
CH <sub>4</sub>	0.48, 0.54, 0.57, 0.6, 0.67, 0.7, 0.73, 0.79, 0.84, 0.86, 0.88, 0.89, 1.69, 7.7
NH <sub>3</sub>	0.55, 0.65, 0.93, 1.5

Table 5.1: Strongest atmospheric absorption bands of carbon dioxide, water, oxygen, ozone, methane and ammonia in the visible to infrared (Source: Tinetti et al. (2009), [crisp.nus.edu.sg](http://crisp.nus.edu.sg)).

The partial pressure tables that I calculated for the different atmospheres were obtained by computing the literature atmospheric abundances according to:  $\log_{10}(N_x/N_H) + 12$ ,

---

with  $N_x$  as the percentage of element  $x$  and  $N_H$  the percentage of hydrogen present to calculate a partial pressure table.

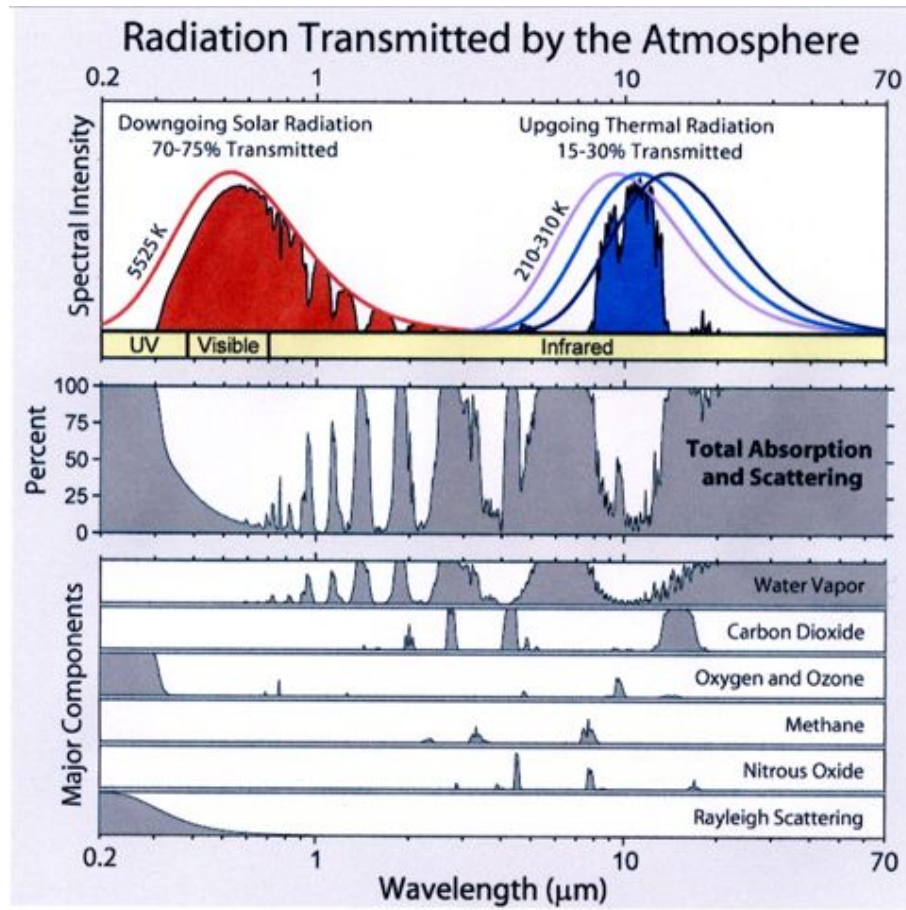


Figure 5.1: *Major absorption bands of Earth's atmospheric compounds. Source: barrettbellamy-climate.com*

The general shape of all Earth-model reflectance spectra (in the optically thin regime) can be explained as follows: The first (blue) large bump consists of the incoming radiation that is reflected back by the planetary surface, affected by the planet's atmospheric absorption bands. As displayed in figure 5.1 and in numbers also in table 5.1, the major absorption bands are from water vapor and carbon dioxide. Depending on the surface albedo, parts of this incoming radiation are stored within the ground. The second bump in the infrared is caused by the outgoing thermal radiation emitted by the surface. In the optically thin regime, the gray surface albedo changes the height of both bumps, or, the amount of reflected light relative to thermal emission. The next chapter introduces the results for the simulations of gray surface albedos on Earths-like planets.

## 5.1 GRAY EARTHS

A gray, non-angular or wavelength dependent surface reflectance basically results in a multiplication of the specific intensities with a constant factor at the surface layer. This determines the amount of the reflected light but does not alter the shape of the spectrum. The energy stored by the surface raises the effective temperature of the planet as opposed to the same planet without irradiation. As the amount of the reflected light decreases, the thermal emission rises and vice versa (figure 5.2). But since the model is spherically symmetric, even for total absorption by the surface, remnants of the incoming light remain in the spectrum. Those are contributed by the tangential characteristics (figure 3.1). The following models for optically thin atmospheres are using the assumption of absorption by the dayside only. For numerical reasons, the surface albedo never reaches zero or unity. The parameters used in this model are Earth-like.

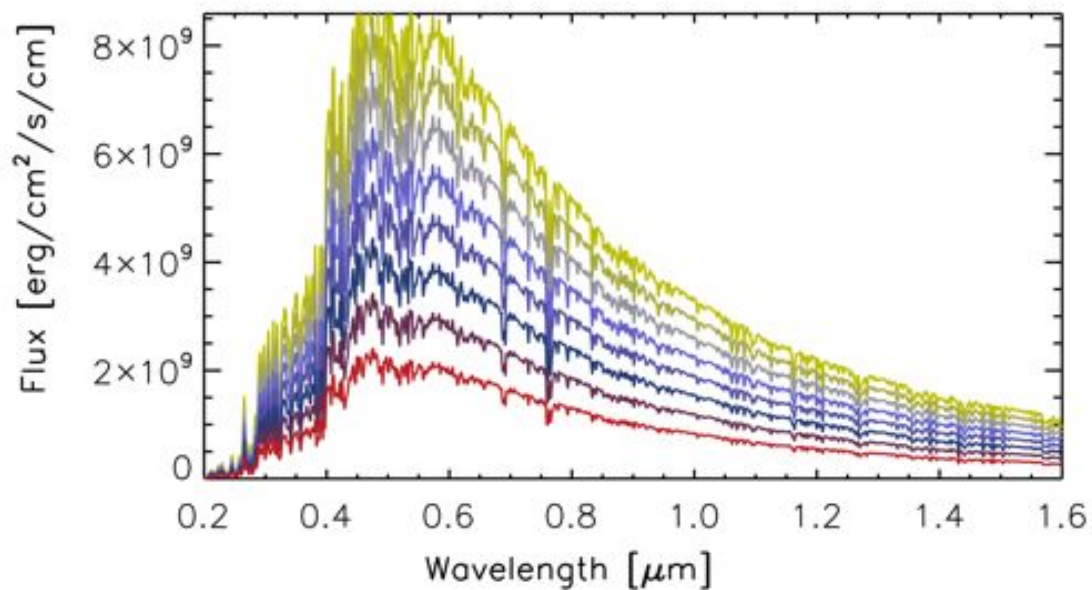


Figure 5.2: *The reflected light in the visible and near infrared for gray surface albedos from  $A = 0.9$  (lightest green) to  $A = 0.2$  (red).*

For these gray models I used the Earth's atmospheric composition, which I will discuss within the next chapter 5.2.1.

## 5.2 THE EARTH-LIKE ATMOSPHERE

The next three subsections treat models with Earth-like parameters, beginning with the atmosphere as it is today and then traveling back in time following the stages of atmospheric evolution as described in chapter 2.3.

### 5.2.1 THE THIRD ATMOSPHERE

The third atmosphere corresponds to the present day Earth atmosphere. The graph 5.3 compares the measured temperature profile to the modeled one. While the pressure curves match fairly well, the temperature curves show an expected deviation. PHOENIX is calculating the atmosphere in chemical and radiative equilibrium. At the moment photochemistry is not included and, therefore, it is not possible to reproduce the thick ozone layer. The temperature decreases monotonically from the surface upwards and does not show an increased temperature within layers that could be assigned to the stratosphere and, thus, to the ozone layer.

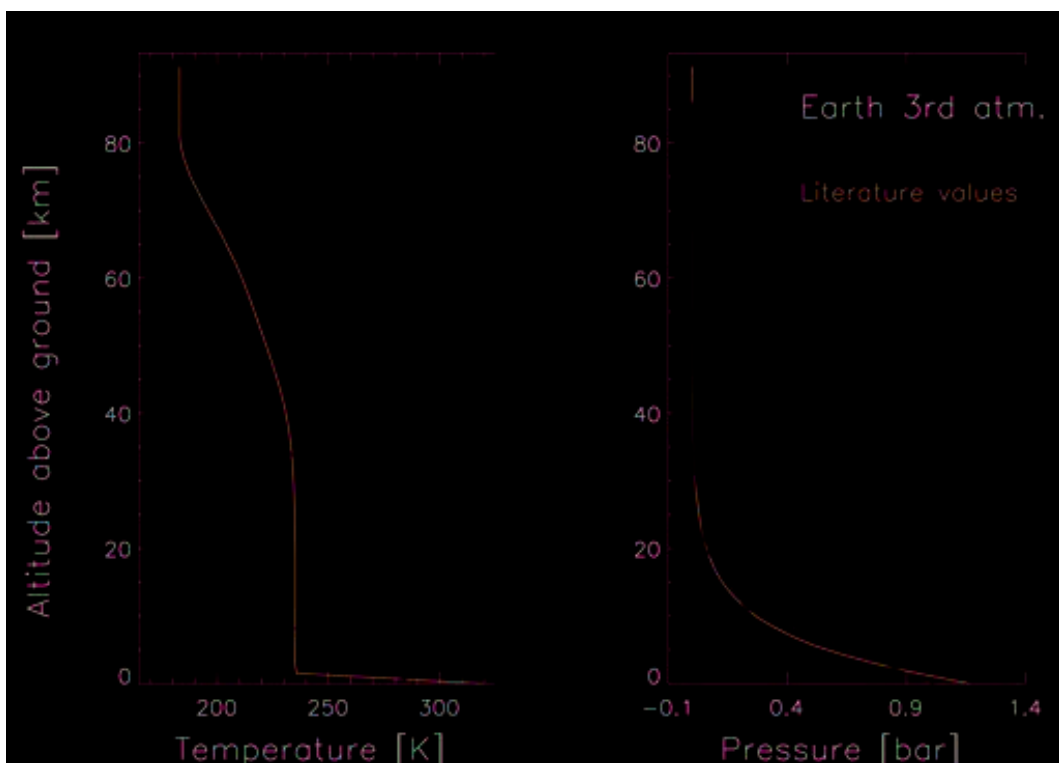


Figure 5.3: A measured temperature and pressure profile of Earth today's atmosphere (red) plotted against the modeled one (yellow). The model cannot reproduce the ozone layer in 1D

The parameters used in this model are:

- $T_{\text{intr}} = 280K$
- Mass =  $5.97 \cdot 10^{24}$  kg, Radius = 6378 km
- Host star: The Sun, heliocentric distance: 1 AU
- Redistribution over day-side only
- Mean Albedo = 0.3

The following table 5.4 shows that the overall chemical composition of the model atmosphere resembles quite nicely the commonly known composition of Earth’s atmosphere. This leads to the question: Is our current atmosphere, at least roughly, in chemical equilibrium? Although the original composition is not fully reproduced, the overall match is good enough to validate the simplified approach that neglects photochemistry and NLTE.

	Earth (lit.)	Model
N <sub>2</sub>	78.08%	77.32%
CO <sub>2</sub>	387 ppm	220 ppm
O <sub>2</sub>	20.95%	20.97%
Ne	18 ppm	35 ppm
Kr	1.14 ppm	1 ppm
Ar	0.93%	1.86%
H <sub>2</sub> O	0-4%	1 ppm

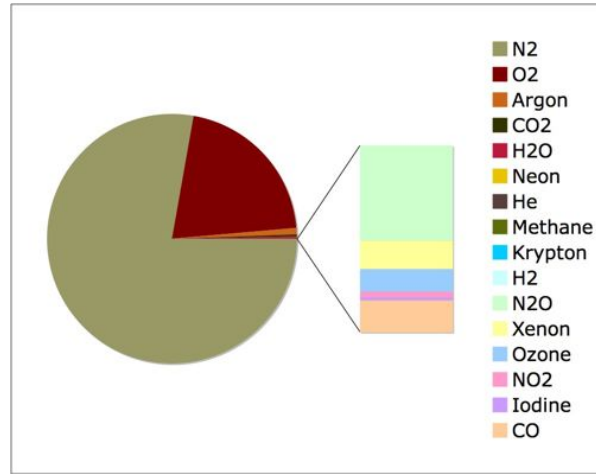


Figure 5.4: Comparison of the measured chemical composition of Earths atmosphere to the modeled one.

Rayleigh scattering results from the interaction of light with molecules in the atmosphere. It is an elastic process of electromagnetic radiation scattering by particles smaller than the wavelength of the light. Rayleigh scattering is inversely proportional to the fourth power of wavelength  $\sim \lambda^{-4}$ , thus shorter wavelengths scatter more than larger ones, causing the Earth’s sky to appear blue. Figure 5.1 illustrates the absorption of light by the major components in Earth’s atmosphere. Figure 5.5 shows the modeled third atmosphere. In

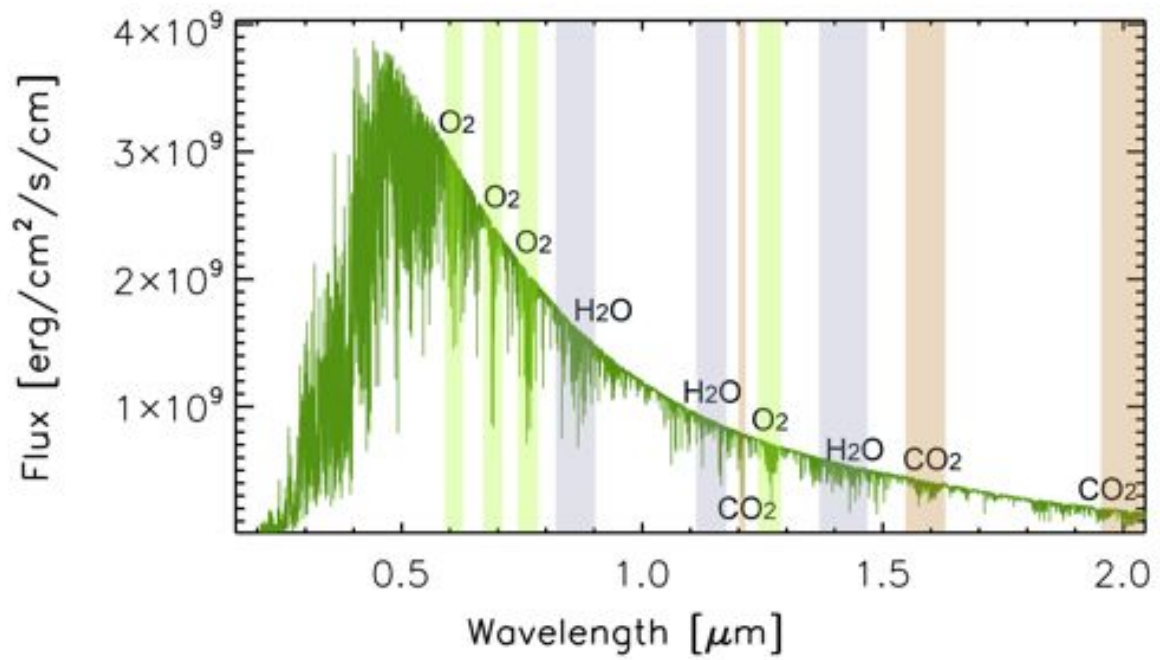


Figure 5.5: *Today's Earth atmosphere.*

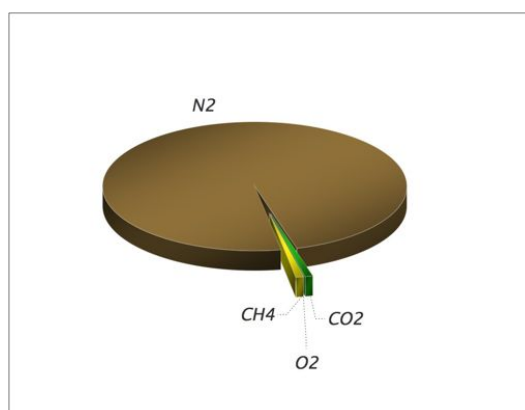
the visible light, strong absorption features are those of oxygen at 0.69 and 0.76  $\mu\text{m}$ . Water vapor absorption bands are dominant in the near infrared.

## 5.2.2 THE SECOND ATMOSPHERE

The second atmosphere represents the burial of carbon and the rise of methane about 2.4 Ga ago. The literature chemical composition used consists of: 98.28 % nitrogen, 1 % carbon dioxide, 0.7 % methane, 0.02% oxygen, again neglecting other species.

The parameters used in this model are the same as in the previous model but with a higher effective temperature of 300K.

	<b>2nd<sub>lit.</sub></b>	<b>2nd<sub>Model</sub></b>
$N_2$	~98.3 %	99.01%
$CO_2$	1 %	0.69%
$O_2$	0.02%	none
$CH_4$	0.7%	0.28 %
$H_2O$	none	159 ppm



The model does not reproduce the literature chemical composition of this atmosphere exactly. The major characteristic of this evolutionary stage, the methane level of 0.7 %, is not reached. But still 0.28 % of methane is enough to produce significant features within the spectrum. An amount of 159 ppm of water vapor is generated. Figure 5.6 shows the simulation result for the second atmosphere, plotted into the infrared range. The red graph results from irradiation with the Solar spectrum, the black line just uses the Solar blackbody as an input. This should facilitate the identification of the absorption signals that stem exclusively from the planetary atmosphere.

The major absorption in the 9 to 14  $\mu\text{m}$  region is due to carbon dioxide and the water vapor that forms in the model atmosphere. Also the methane absorption feature at 7.7 $\mu\text{m}$  can be seen. A very dominant feature occurs in the visible light from 0.53 to 0.64  $\mu\text{m}$ . The linelists used here are of the HITRAN 2004 catalogue. This means real measured data, that seems to end at the beginning and end of this feature, creating sharp edges.

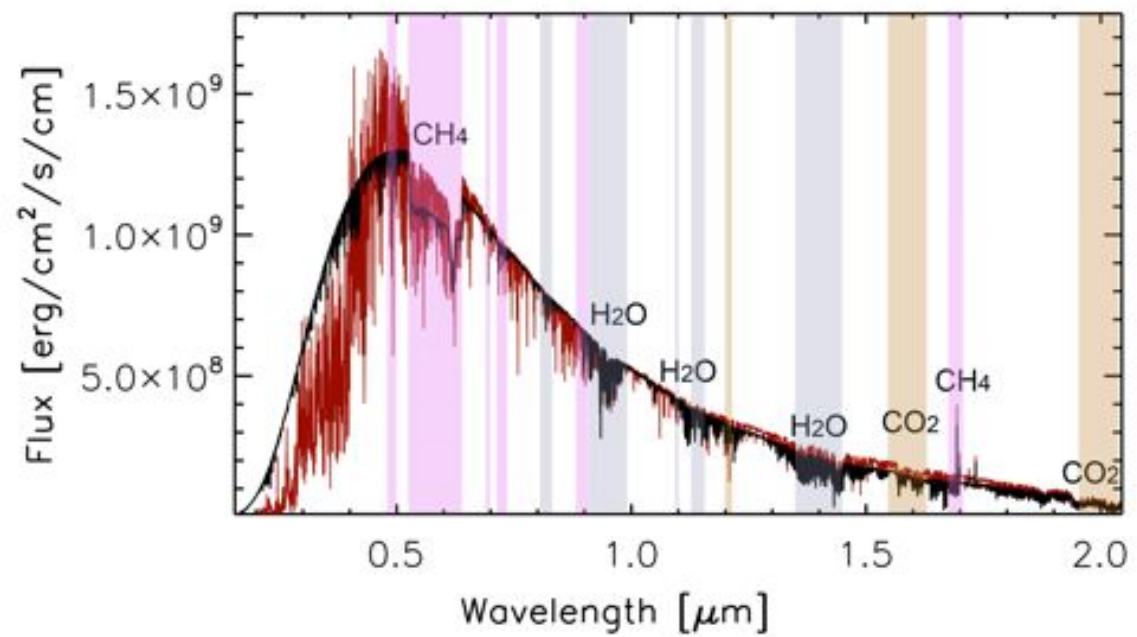


Figure 5.6: *The atmosphere of the second epoch is dominated by methane and carbon dioxide absorption features.*

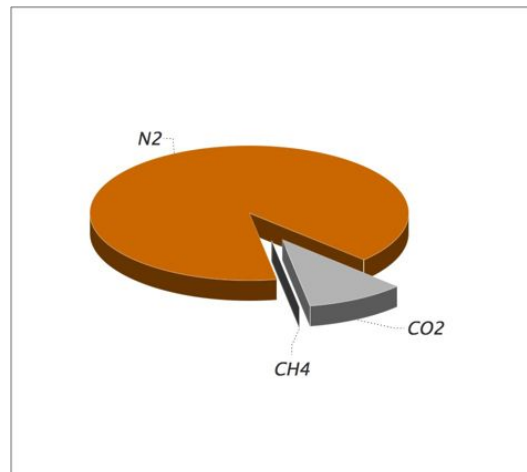
### 5.2.3 THE FIRST ATMOSPHERE

The atmospheric composition for the atmosphere at the end of the late heavy bombardment period is chosen according to Kaltenegger et al. (2006a). About 3.9 Ga ago, the atmosphere consists of nearly 90% nitrogen, 10% and 1.79 ppm of methane, other molecules are neglected.

The parameters used in this model are:

- $T_{\text{intr}} = 450K$
- $M_{\text{Earth}} = 3 \cdot 10^{-6}M_{\odot}$ ,  $R_{\text{Earth}} = 6378 \text{ km}$
- Host star: The Sun, heliocentric distance: 1 AU
- Mean Albedo = 0.1

	<b>1st<sub>lit.</sub></b>	<b>1st<sub>Model</sub></b>
$N_2$	~89 %	92.93%
$CO_2$	10 %	7.04%
$CH_4$	18 ppm	72 ppm
$O_2$	none	
$H_2O$	none	



I chose a high effective temperature for this model, based on the time estimate of Kasting (1993). The surface was still too hot ( $T_{\text{intr}} = 450K$ ) for the oceans to form, that happened about 100 million years later. For the surface reflectance I assumed a low value of 0.1. Lava has a very low albedo of  $A \sim 0.004$ , but since the crust probably was not solid yet, I chose a slightly higher albedo value. The literature values of the chemical composition of the atmosphere are reproduced fairly well by the code, resulting in a deviation of roughly 3 % in nitrogen and carbon dioxide and a four times higher methane level, see table 5.2.3. In figure 5.7, the absorption features of CO<sub>2</sub> can be seen at 1.21, 1.57 and 1.6 $\mu\text{m}$ . Again the colored (blue) spectrum results from a full Solar input spectrum, the black from a blackbody.

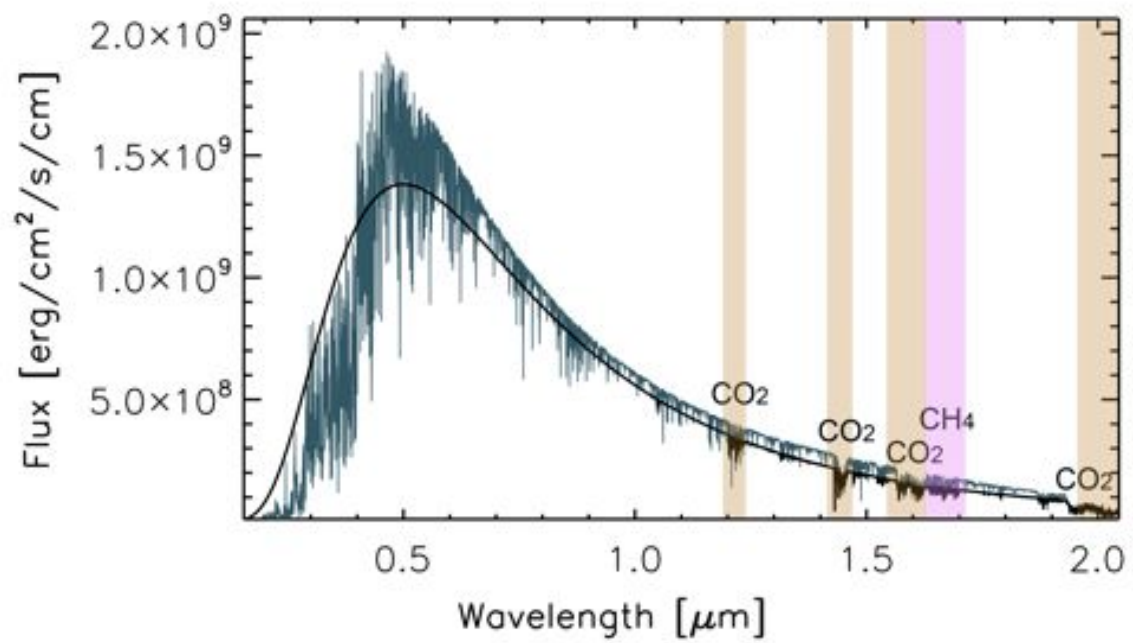


Figure 5.7: *Earth's first atmosphere in the visible to mid infrared light. The blue curve is the reflectance spectrum that contains the solar spectrum as an input, the black curve solely the solar blackbody.*

### 5.3 THE VENUS-LIKE ATMOSPHERE

Venus atmosphere is hot, dry and optically thick, about 100 times denser than Earth's atmosphere. With a surface temperature of  $\sim 740$  K and a surface pressure of 93 bar, Venus shows no signs of life. The two main atmospheric gases are  $\text{CO}_2$  and N and traces of sulfur dioxide, argon and water. Venus is rotating slow and retrograde, one rotation around its axis takes 116 Earth-days. The strong winds in Venus upper atmosphere cause these upper layers to rotate up to 60 times faster than the planet is rotating underneath them. This wind speed is decreasing towards the ground to a slight breeze but the thick atmosphere and the strong zonal winds are responsible for a low day- to nightside temperature contrast.

Venus lacks a magnetic field, the only weak shelter from the solar wind is provided by Venus ionosphere ("induced magnetosphere"). With this non-sufficient shielding and a heliocentric distance of 0.7 AU, Venus lost its hydrogen to space by photodissociation. If Venus atmosphere had been more Earth-like in the past, the present greenhouse gases and the water loss would have led to a runaway greenhouse effect. The most life-friendly place is situated at about 50 km above the surface, where pressure and temperature are similar to Earth's at sea level.

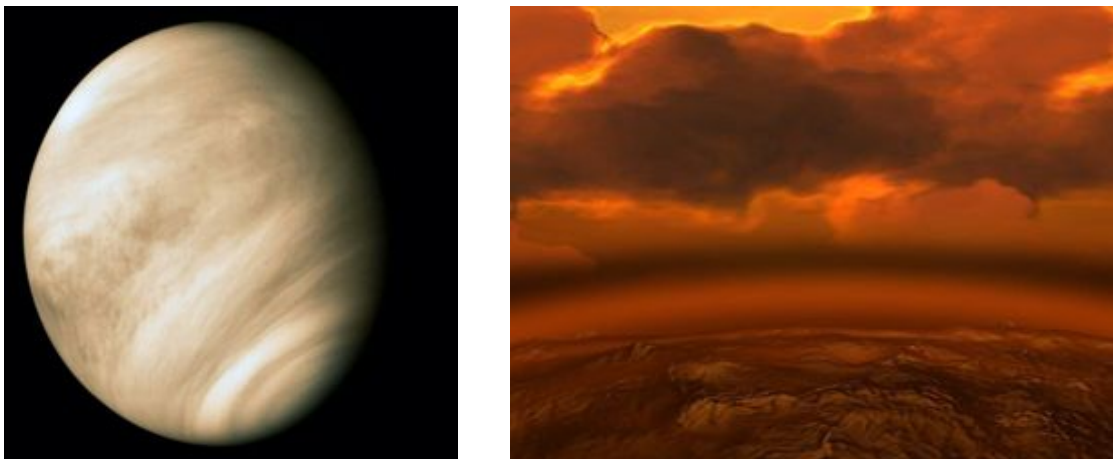


Figure 5.8: *Venus atmosphere is optically thick and contains about 93 times more mass than Earths atmosphere. Picture sources: NASA (left), ESA (right).*

The parameters used in this model are:

- $T_{\text{surface}} = 740K$
- Mass =  $4.87 \cdot 10^{24}$  kg, Radius = 6050 km
- Host star: The Sun, heliocentric distance: 0.72 AU
- Optically thick

	Venus (lit.)	Model
$CO_2$	96.5%	95.49%
$N_2$	3.5%	4.47%
$SO_2$	150 ppm	150 ppm (at surface)
$Ar$	70 ppm	218 ppm (at surface)
$H_2O$	20 ppm	29 ppm (at surface)
$CO$	17 ppm	dep. on height
$He$	12 ppm	none
$Ne$	7ppm	26 ppm (at surface)

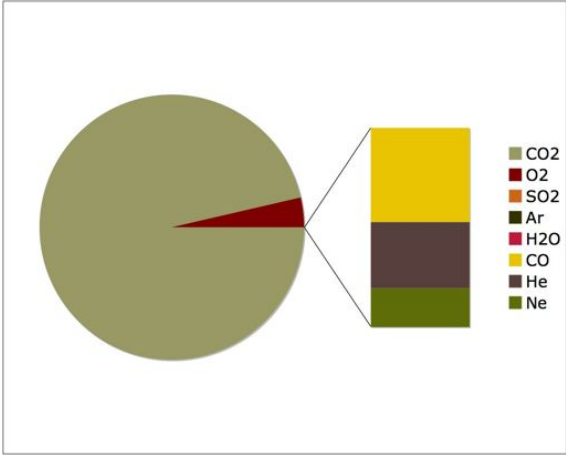


Figure 5.9: Comparison of the measured chemical composition of Venus atmosphere to the modeled one.

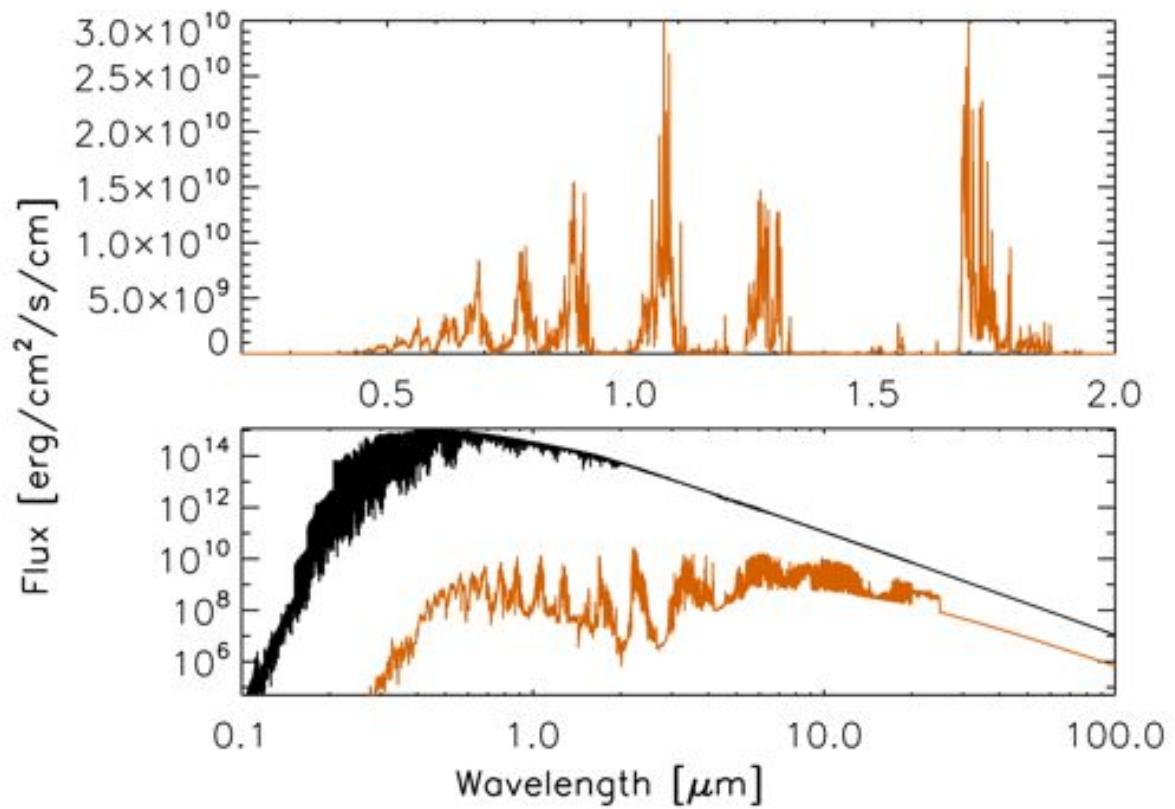


Figure 5.10: *Comparison of the measured chemical composition of Venus atmosphere to the modeled one.*

## 5.4 HYPOTHETICAL SUPER-EARTH

Gliese 581 is a red dwarf star with spectral type M3V in the constellation Libra with an estimated mass of  $M_{\text{Sun}} \sim 1/3$ . In 2007, Gliese 581c, the first low mass planet close to the habitable zone was discovered. So far, Gliese 581 is confirmed to have 4 planets, Gliese 581b,c,d and e. In September 2010, Steven S. Vogt and R. Paul Butler (Vogt et al. (2010)) combined 122 observations from HIRES<sup>1</sup> with 119 measurements from the HARPS<sup>2</sup> instrument and claimed 2 more possible exoplanets, Gliese 581g and f. Francesco Pepe (Geneva Observatory) re-analyzed HARPS measurements and could not find any of the two planets (Mullen (2010)).

If Gliese 581g existed, it would have orbited its host star within the habitable zone with an orbital period of 37 days. Its was believed to range in mass in between 3.1 to 4.3 Earth masses (depending on its core) and 1.3 to 2.0  $R_{\text{Earth}}$  allowing it to keep a dense atmosphere.

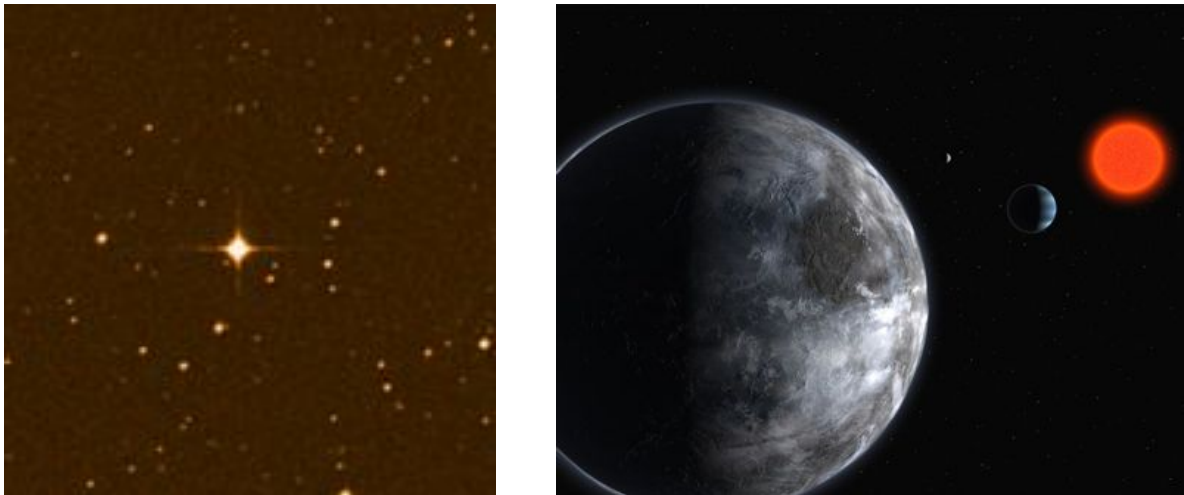


Figure 5.11: *The red dwarf star Gliese 581 (ESO Online Digitized Sky Survey) and an artists impression of an exoplanet within the habitable zone (by ESO).*

Anyway, I chose to take a closer look at this hypothetical exoplanet and used the suggested parameters to model the object. I simulated an optically thick version of this inscrutable planet using solar abundances.

---

<sup>1</sup>High Resolution Echelle Spectrometer instrument of the Keck 1 telescope

<sup>2</sup>High Accuracy Radial Velocity Planet Searcher, European Southern Observatory's 3.6 m telescope at La Silla Observatory

The parameters used in this model are:

- Mass =  $5.97 \cdot 10^{24}$  kg, Radius = 8291 km
- Host star: Red dwarf (3200 K), heliocentric distance: 0.146 AU
- Optically thick

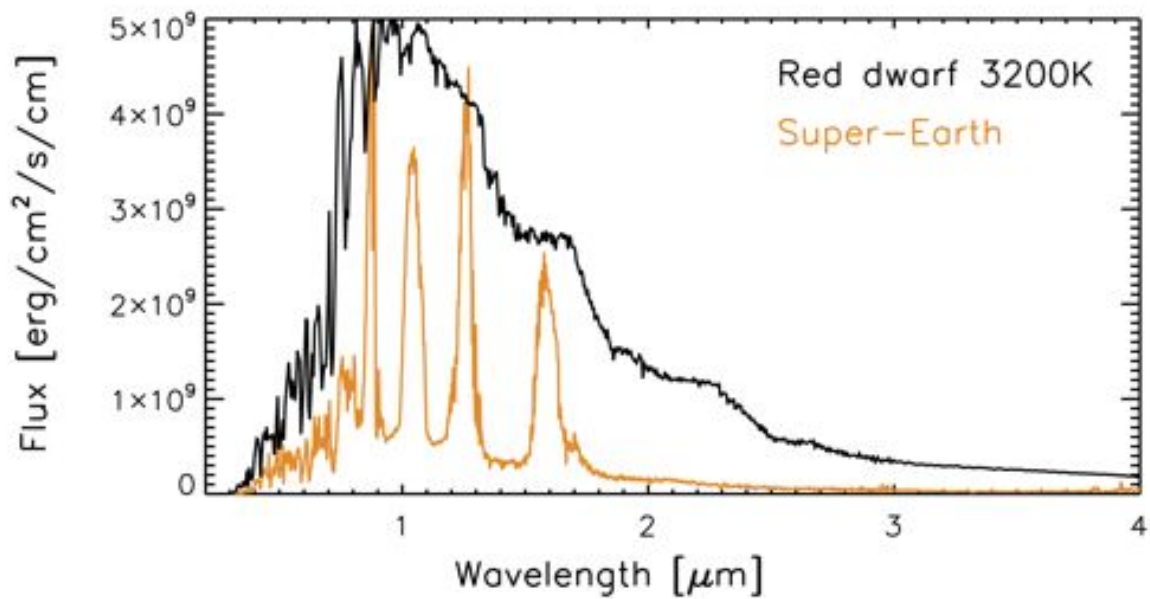


Figure 5.12: *The spectrum of a Super-Earth with Gliese 581g-like parameters around an M dwarf of 3200 K.*

Figure 5.12 displays the result of the simulation. The host star's spectrum is printed in black, this star is a red dwarf with Gliese 581-like parameters. The super-Earth has a dense atmosphere, the surface pressure amounts to  $\sim 200$  bars and the surface temperature is about five times hotter than on Earth. The model did not converge for Earth-like or Venus-like atmospheric compositions.

## 5.5 STEAMY WORLD GJ1214 b

In 2009, the super-Earth GJ1214 b was discovered by Zachory Berta, a graduate student working on the MEarth Project, a survey that photometrically monitors 2000 nearby M dwarfs (Nutzman & Charbonneau (2008)). In particular, MEarth is looking for exoplanets that are located within the habitable zone. With a rotation period of 1.6 days, GJ1214 b orbits its host star, the red dwarf GJ1214, located 40 light years away in Ophiuchus. GJ1214 b has a radius of  $\sim 6.6$  times that of the Earth and its mass is estimated to be  $\sim 2.6 \cdot M_{\text{Earth}}$ .

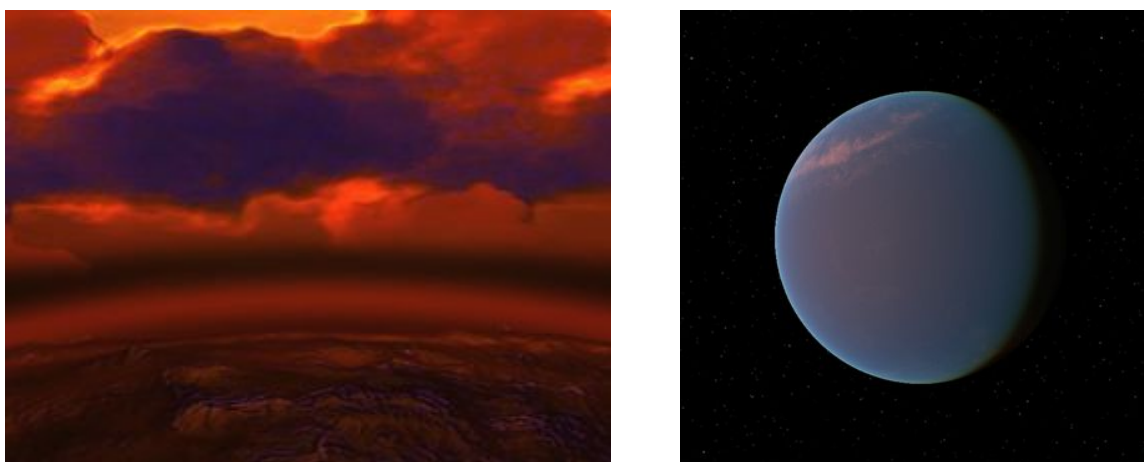


Figure 5.13: *Artists impressions of GJ1214 b. Left image: A modified image of a dense cloud atmosphere (Image: ESA). The right hand picture shows an image of this steamy exoplanet (source: solar-flux.forumandco.com)*

GJ1214 b is assumed to be a kind of water world. The group around Jacob Bean measured the transmission spectra of this super-Earth with the FORS2 instrument on the UT1 telescope of the Very Large Telescope, on April, 29th and June, 6th 2010 (Bean et al. (2010)). They fitted different atmospheric compositions to measured spectra, a solar composition one, a 100 % water and a 70 %  $\text{H}_2\text{O}$  + 30 %  $\text{H}_2$  atmosphere. They suggested an atmosphere that was composed of at least 70% water vapor. But with a semimajor axis of 0.0143 AU (and eccentricity of  $< 0.27$ ) GJ1214 b's equilibrium temperature ranges in between 400 and 550 K, which is too hot for water to be liquid. Thus, GJ1214 b seems to be a steamy world but not an ocean planet.

The parameters used in this model are:

- $T_{\text{eff}} = 470K$
- Mass =  $3.94 \cdot 10^{25}$  kg, Radius = 17200 km
- Host star: M dwarf 2700K, astrocentric distance: 0.068 AU

For the simulation I chose a 100 % water vapor atmosphere. The surface temperature reaches  $\sim 800$  K. The simulation result is shown in figure 5.14. The lower plot shows a full spectrum with logarithmic x- and y-axes. The black graph represents the red dwarf input spectrum. I overlaid a part of figure 5.1 which shows the bands of water vapor absorption to figure 5.14. This direct comparison makes it easy to see that the model works very well. The emerging spectrum is dominated by water vapor absorption. From  $20 \mu\text{m}$  on, this spectrum is calculated with a lower resolution.

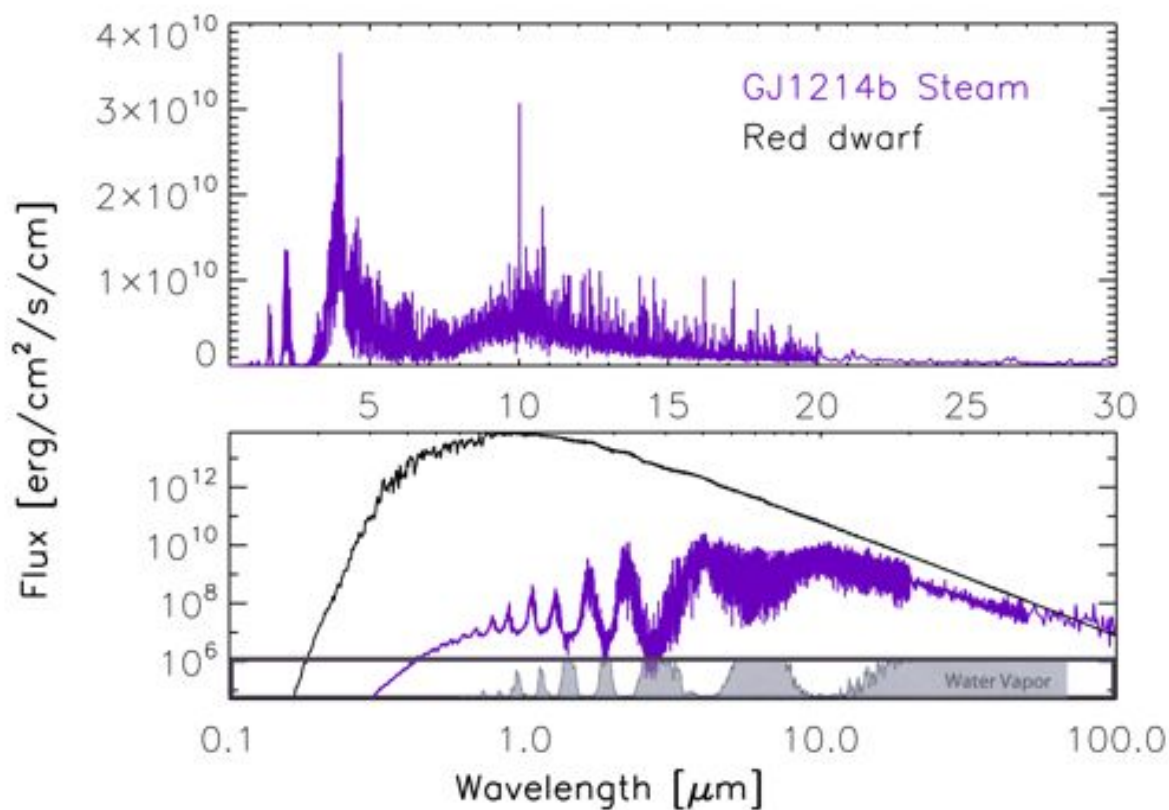


Figure 5.14: *The model of GJ1214 b with a 100% water vapor atmosphere. Black: Host star GJ1214, Violet: Super-Earth GJ1214 b. Inserted into the plot are the water vapor absorption bands taken from figure 5.1.*

## 5.6 OCEAN PLANET

Contrary to GJ1214 b, this model represents a true ocean planet. It is completely and homogeneously covered by an ocean of water. The atmosphere is optically thin, clouds are neglected. Of course an ocean planet is not very likely to be cloudless. But mapping the surface with cloud patterns is a subject to upcoming 3D simulations. This model focusses on the reproduction of the angular albedo of the liquid surface. The effective temperature is determined by the amount of energy stored by the water surface and here the calculation of the overall albedo, that is needed as an input parameter for the temperature correction, is performed differently. The water is considered to be pure and colorless.



Figure 5.15: *An ocean planet orbiting at the right heliocentric distance for water to be in the liquid form.*

The parameters used in this model are:

- $T_{\text{surface}} = 327K$
- Mass =  $5.97 \cdot 10^{24}$  kg, Radius = 6378 km
- Host star: The Sun, heliocentric distance: 1 AU
- Mean Albedo = 0.103
- Atmospheric composition: Today's Earth

Plot 5.16 shows the result for the calculation of the Fresnel reflectivity. The absorption features are the same as described in chapter 5.2.1.

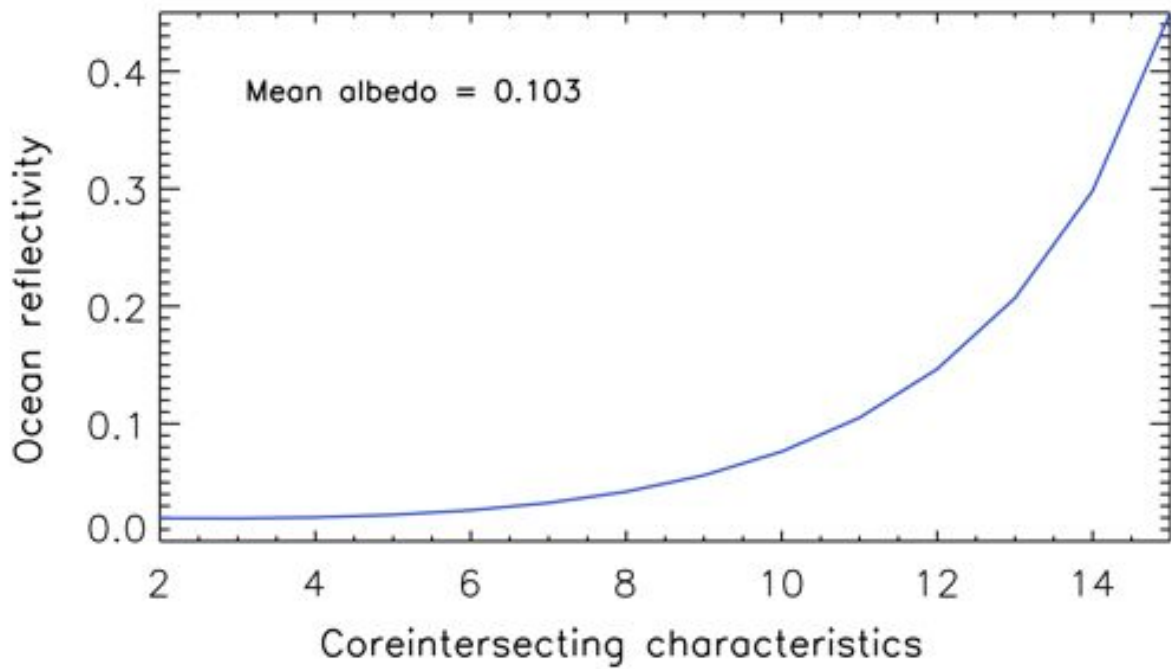


Figure 5.16: *The angular dependent albedo.*

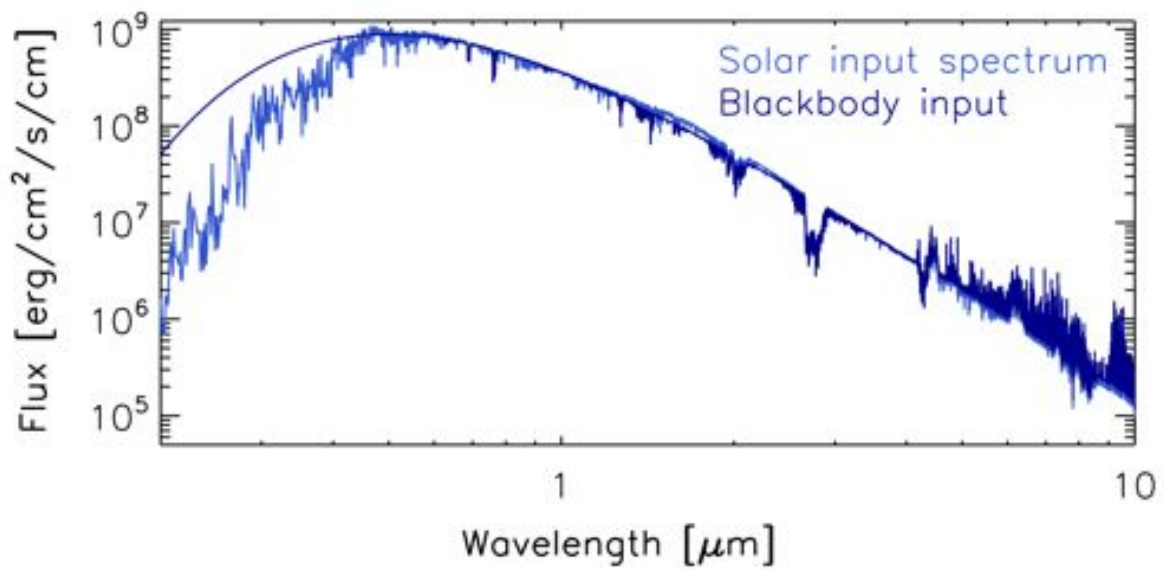


Figure 5.17: *The spectrum of a “gray” water planet basically resembles the gray Earth, the overall albedo is a result of the atmospheric height.*

## 5.7 SNOWBALL PLANET

This scenario describes the coldest global climate possible. A rocky exoplanet completely covered by fresh snow. I chose to name this chapter the snowball planet since the term "snowball earth" is already occupied: The Snowball Earth hypothesis "proposes that the glacial deposits were formed by a global glaciation that occurred when ice advanced past a critical latitude ( $30^\circ$  North and South), creating a runaway ice-albedo feedback" (Schrage et al. (2002)).

Since most of the incoming radiation would be reflected back to space by the snowy surface, the global mean temperature would be about  $\sim 220K$  on Earth in average and about  $\sim 250K$  at the equator. Still the ocean would even out the latitudinal temperature gradient. The modeled snowball planet does not have an ocean. It is completely covered by (fresh) snow. The climate of such a world would be dry and cold. The ice and snow could directly sublime into the atmosphere without ever melting.

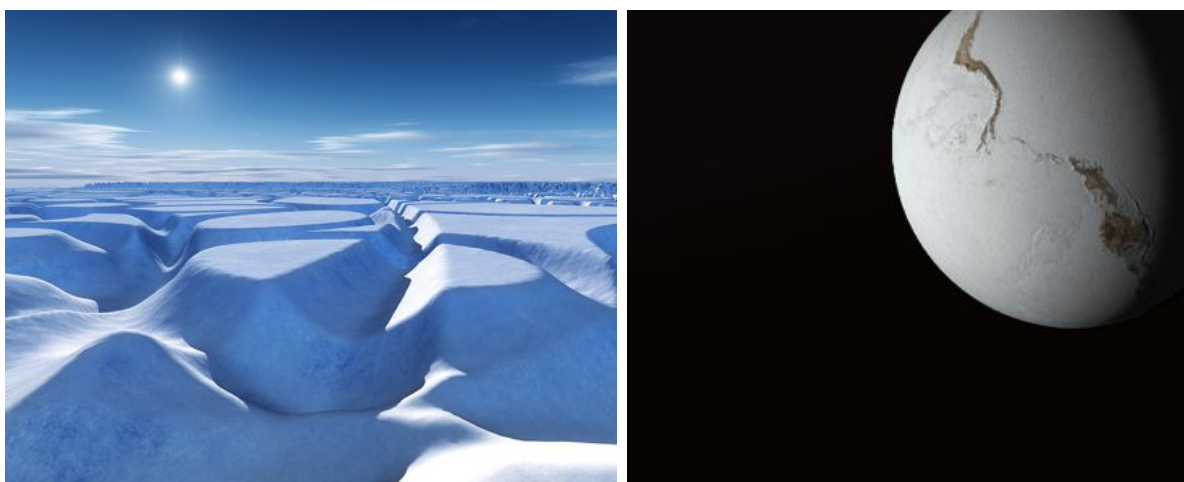


Figure 5.18: *The snowball planet (original pictures: 3Dsceneries.com and celestiamotherlode.net)*

The parameters used in this model are:

- $T_{\text{surface}} \sim 0^\circ C$
- Mass =  $5.97 \cdot 10^{24}$  kg, Radius = 6378 km
- Host star: The Sun, heliocentric distance: 1 AU
- Atmospheric composition: Today's Earth

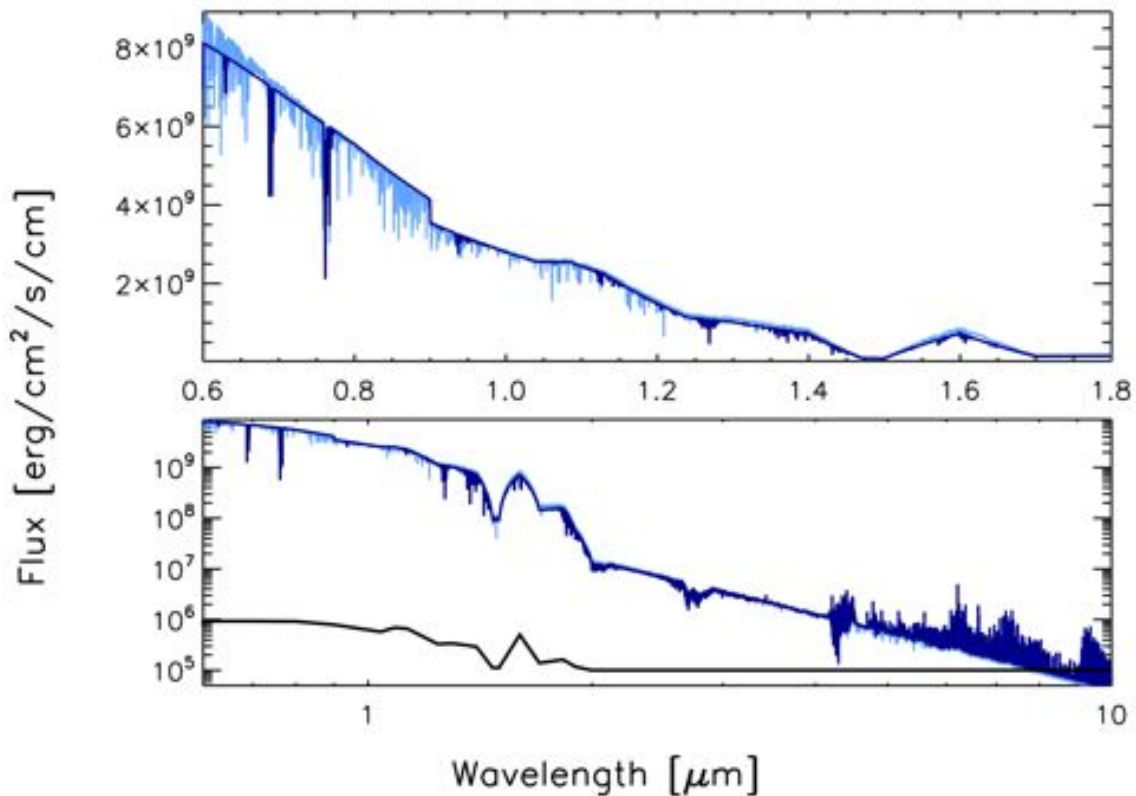


Figure 5.19: *Upper: Spectrum of the snowball planet. Lower: Logarithmic figure with albedo curve (black).*

Figure 5.19 displays the model outcome for the snowball planet. The absorption bands are the same as in the case for figure 5.5, therefore I will not mention them again here. The upper graph of the plot shows the visible to near infrared region, the lower logarithmic plot is extended into the mid IR region. The light blue spectrum is a result of a full Solar input spectrum, the darker blue one just uses a blackbody as an input. The black line represents the wavelength dependent albedo curve which is scaled by an arbitrary factor to fit into the plot. Figure 5.19 confirms that the model responds very well to the implemented lower boundary condition for the wavelength dependent albedo.

## 5.8 DESERT (MARTIAN) PLANET

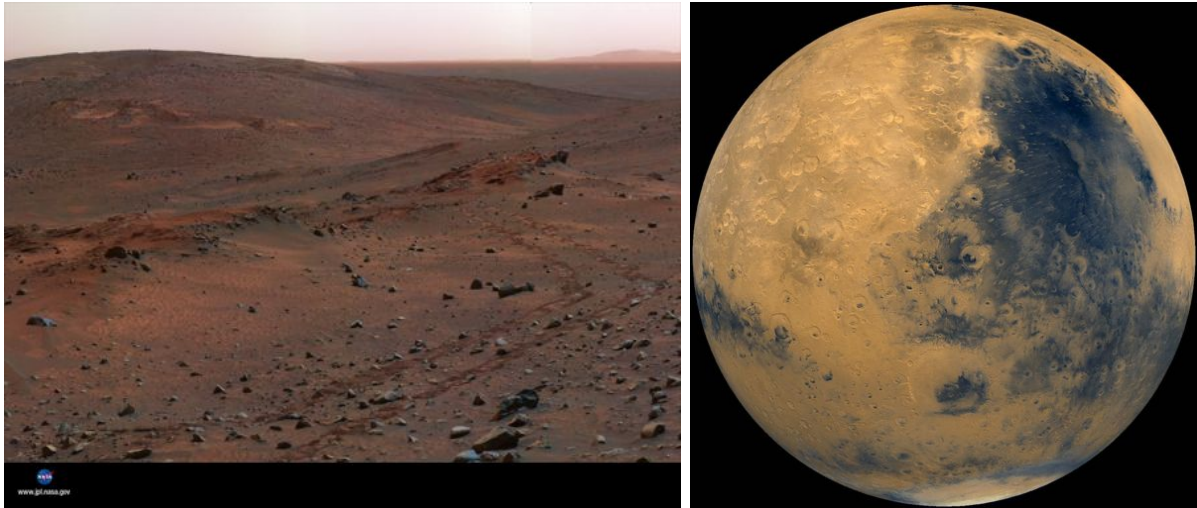


Figure 5.20: *Left: On April 3, 2005, Mars Rover “Spirit” took this image (assembly from different frames). It shows a region in the ‘Columbia Hills’. Right: Assembly of 100 red and violet filter images of the Viking orbiter, taken in 1980 during early northern summer on Mars. The image shows the Syrtis Major hemisphere of Mars as seen from 2000 kilometers above the surface. Source: NASA*

A terrestrial planet, solely covered by sand and rocks with a thin atmosphere will probably be a place hostile to life. Our neighbor planet Mars is a good example of such a planet. Its mass is about  $0.1 \cdot M_{\text{Earth}}$ . With an eccentricity of  $e = 0.09$  Mars orbits the Sun within 1.38 AE and 1.67 AE in 687 days.

The atmosphere is very thin and the average surface pressure amounts to only about 0.006 bar (sea level on Earth  $\sim 1$  bar). The surface structure of Mars is dominated by large impact craters and plains that formed during the late heavy bombardment period. The “red planet” owes its name to iron(III) oxide (hematite, or rust).

The surface albedo data used here has been described in chapter 3.1.2. Figure 5.21 shows the result. Unfortunately the attempt to rebuilt the martian atmosphere failed. In general it should be possible to recreate it, but the model did not converge in time. I used the Earth’s atmospheric composition.

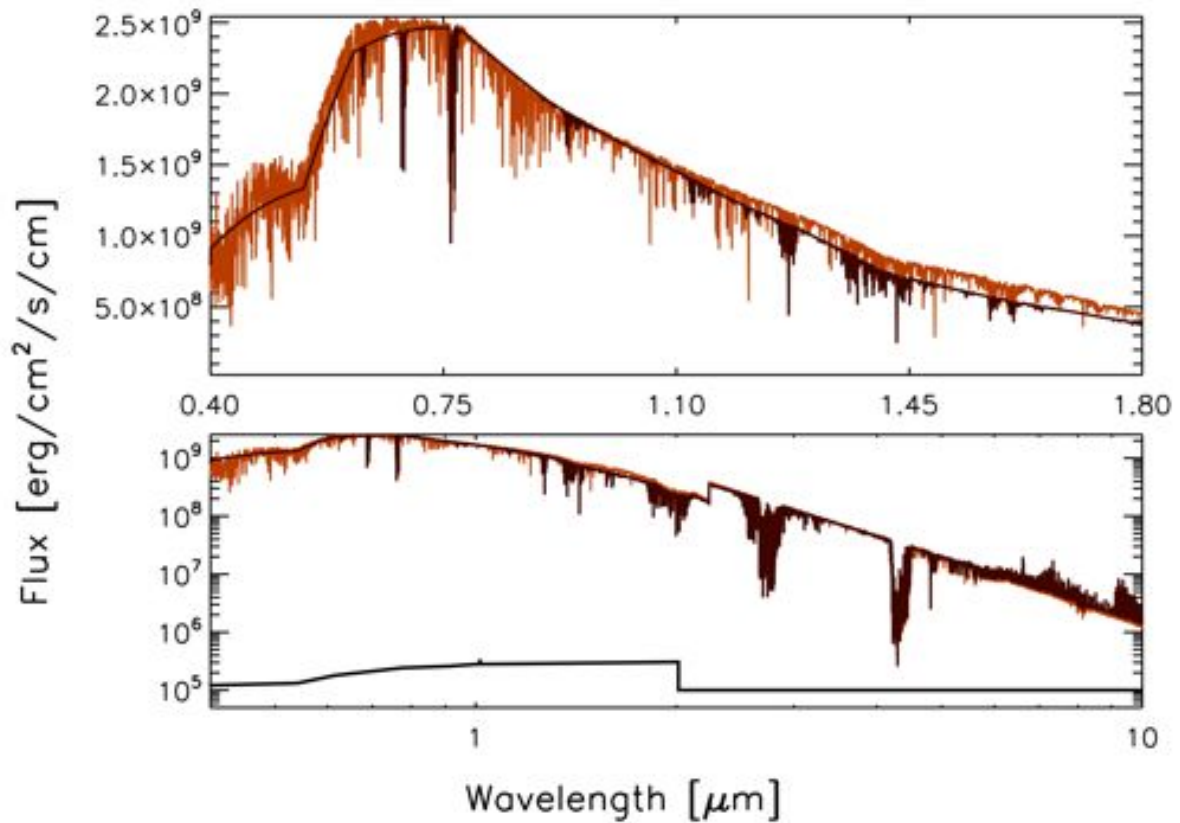


Figure 5.21: *Upper: Visible to near IR spectrum of the desert planet. Lower: Logarithmic plot into the mid IR range. The reflectance spectrum with Solar input spectrum is plotted in light brown, dark brown in case of a BB input spectrum and the surface albedo curve (black).*

The planet has a surface temperature of 310 K and an Earth-like surface pressure. The albedo curve is quite smooth and lacks dominant features. This can also be seen in the resulting reflectance spectrum (figure 5.21).

## 5.9 JUNGLE PLANET



Figure 5.22: *Left: The unbroken rainforest (billofthebirds.blogspot.com). Right: An impression of a jungle world (original picture: doogsy.deviantart.com)*

The modeled green planet has the same parameters as Earth but is completely covered by plants. In opposition to the atmospheric bioindicators, the vegetation red edge is a true surface biosignature. Chlorophyll absorbs at visible and UV, chlorophyll A at 430 nm and 662 nm and chlorophyll B at 453 nm and 642 nm. Reflection occurs between 700 nm and 1000 nm to protect the plant from overheating and thus to prevent the loss of chlorophyll. Chlorophyll is not restricted to the land only. It also occurs in the oceans where phytoplankton is present. The strongest concentrations of chlorophyll in the oceans are measured in areas where cold water is upwelling, bringing nutrients from the ocean floor. On Earth, the strongest signals in the open water are located in the Atlantic Ocean close to the Equator due to the easterly trade winds (Seager et al. (2005)).

Wolstencroft & Raven (2002) proposed that planets around cooler stars might develop another kind of vegetation red edge but shifted to longer wavelengths. Earth's vegetation red edge has not been seen by any space based mission yet. That is also due to the fact that Earth is by far not fully covered by plants.

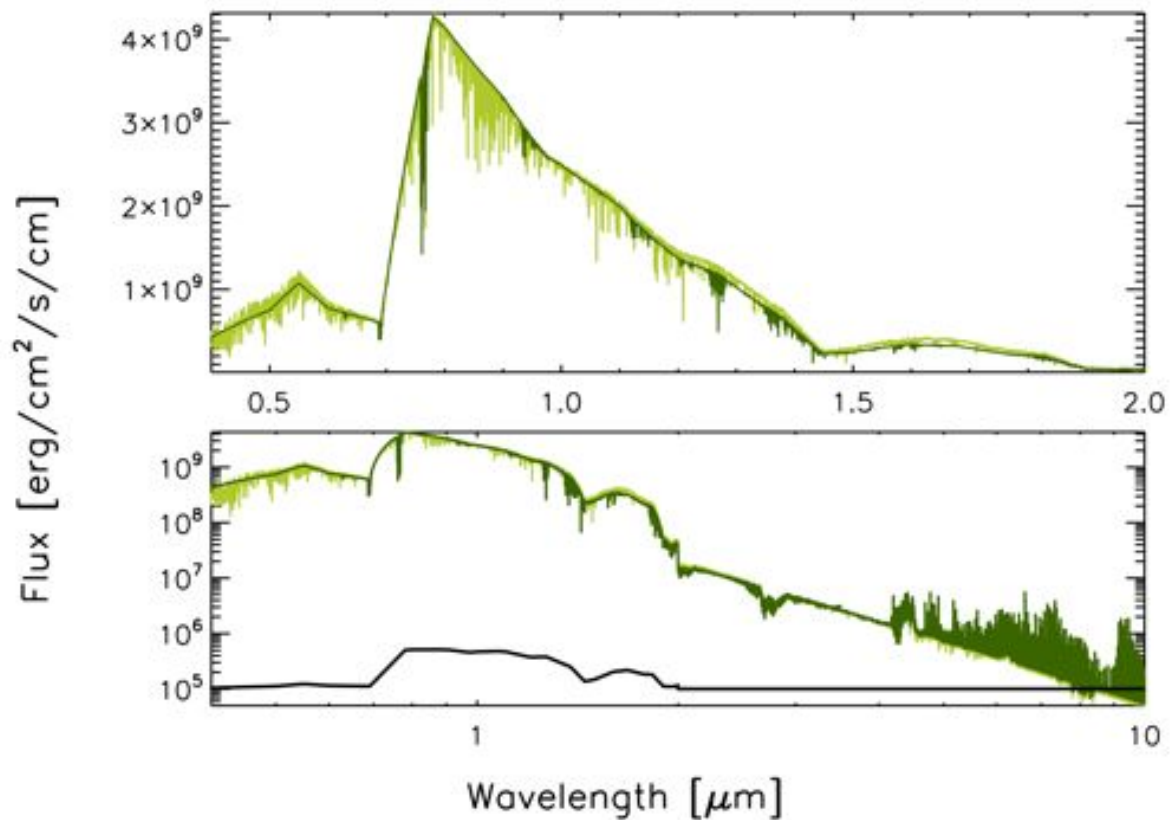


Figure 5.23: *Left: Full spectrum of the desert planet. Right: The part of the spectrum that JWST would be able to detect.*

The planet recreated here is fully covered by plants and thus exhibits a strong vegetation red edge signature (figure 5.23). Out of all three cases, the snowball, the desert and the jungle (or forest) world, the jungle world has the most dominant surface feature.

---

# Chapter 6

## PHOTOMETRY

What kind of instrument would be needed to see the surfaces signatures of the snowball, the desert or the jungle planet in the reflected light?

Here I want to introduce a way to get a first estimate. In the following I do not want to take a look at single lines, not even molecular bands. This is rather a very simple investigation to answer the question, whether the dominant features like the sharp rise in reflectance in the case of the vegetation red edge (figure 5.23) could be seen. This approach should be seen as a “proof of concept”, not as a realistic photometric simulation.

I suggest filters, that are inspired by those of the NIRSpec onboard JWST with an additional one within the visible wavelength range. The filters I chose are named Filter A,B and C:

<b>JWST filter</b>	<b><math>\lambda</math>-range [<math>\mu\text{m}</math>]</b>	<b>Model filter</b>	<b><math>\lambda</math>-range [<math>\mu\text{m}</math>]</b>
no filter		Filter A	$0.5 \leq \lambda \leq 0.7$
F070LP	$0.7 \leq \lambda \leq 1.2$	Filter B	$0.7 \leq \lambda \leq 1.0$
F100LP	$1.0 \leq \lambda \leq 1.8$	Filter C	$1.0 \leq \lambda \leq 1.7$

Figure 6.1: *Filter functions of the NIRSpec filters on JWST (stsci.edu/jwst/instruments/nirspec) and simple filters adapted for a first photometric estimate.*

The wavelength dependent surface albedo data ranges in between:

- Snowball planet  $\rightarrow 0.6\mu\text{m} \leq \lambda \leq 2\mu\text{m}$
- Desert planet  $\rightarrow 0.4\mu\text{m} \leq \lambda \leq 2\mu\text{m}$
- Jungle planet  $\rightarrow 0.4\mu\text{m} \leq \lambda \leq 2\mu\text{m}$

The spectrum of the snowball planet resembles the spectrum of the gray planets within the range of filter A, that I suggest should range from  $0.6\mu\text{m} \leq \lambda \leq 0.7\mu\text{m}$ . The lower filter range is limited by the missing albedo data below  $0.6\mu\text{m}$ . The snowball planet will not be easy to distinguish from a bright but gray object. The deviations from a gray planet are most noticeable within filter C.

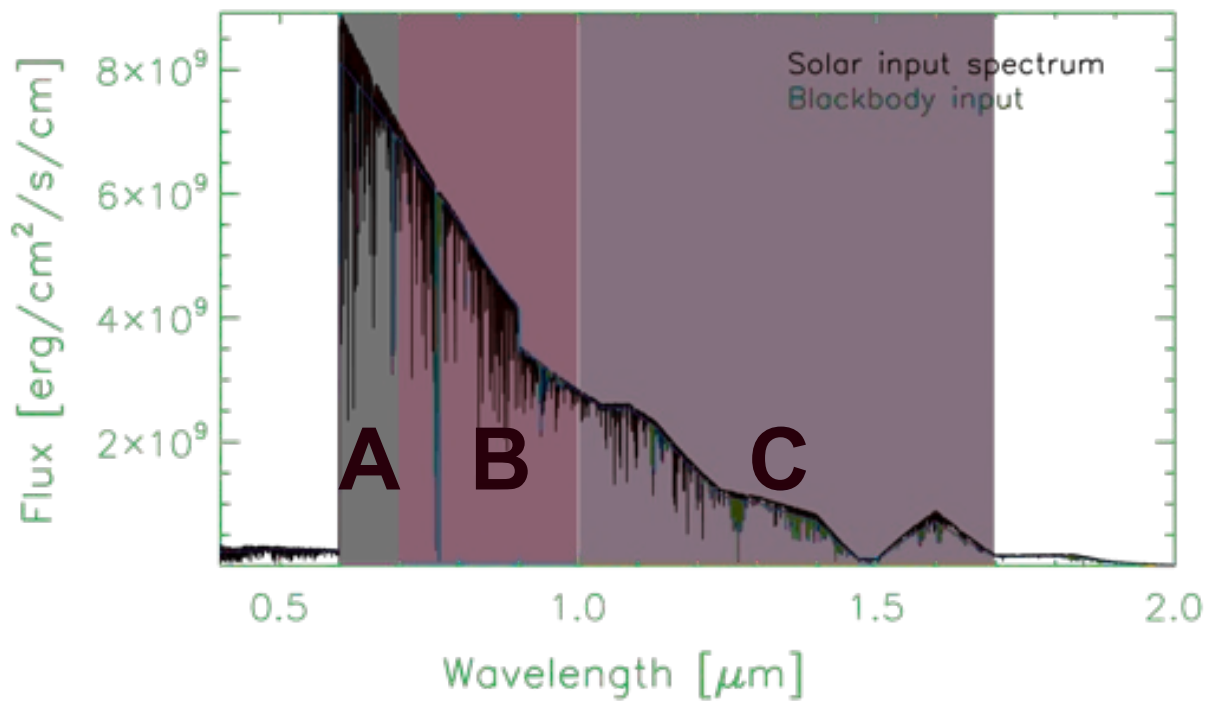


Figure 6.2: *The snowball planet, overlaid by the model filters A,B and C as described in table 6.1.*

---

In case of the desert planet I would suggest a filter A that ranges from  $0.5\mu\text{m} \leq \lambda \leq 0.7\mu\text{m}$ . Figure 6.3 displays the desert planet spectrum and the suggestion for the filter ranges.

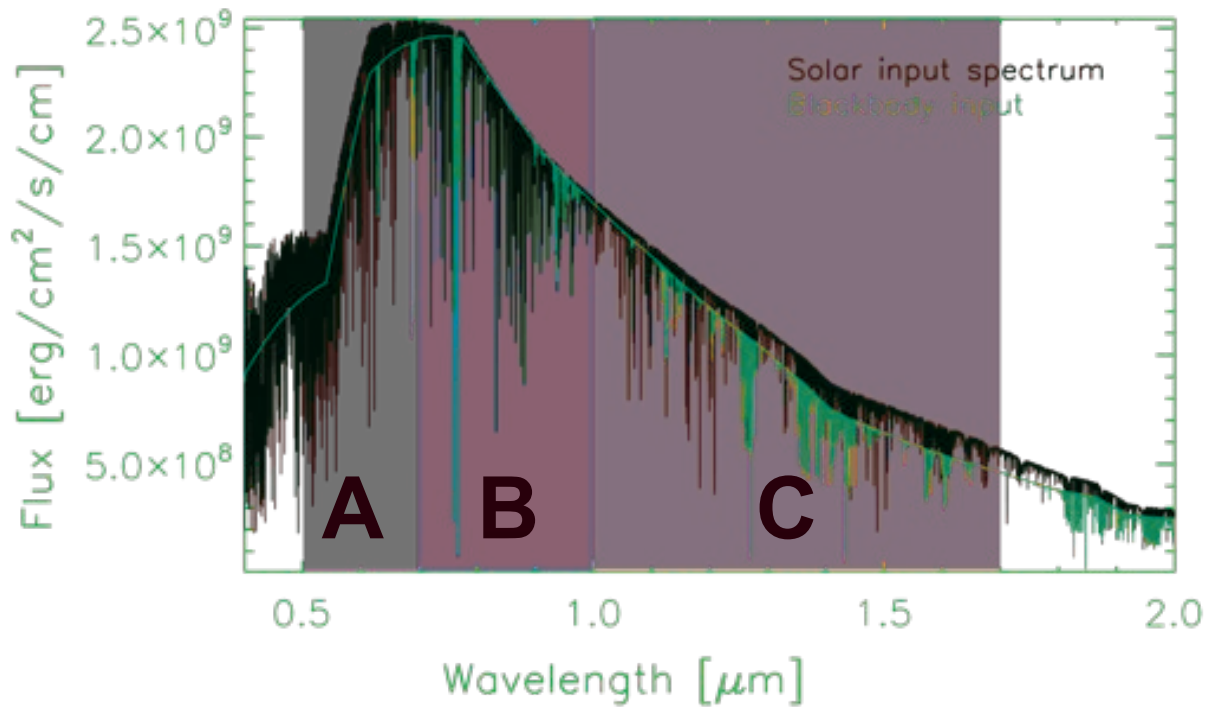


Figure 6.3: *The desert planet, overlaid by the model filters A,B and C.*

As already mentioned in the previous chapter, the modification by the surface reflectance does not alter the shape of the spectrum radically. But there is a change in reflectance at  $\sim 0.55 \mu\text{m}$  that creates a smooth edge in the spectrum. To include this edge, filter A should cover a larger wavelength range than in case of the snowball or the jungle world.

Figure 6.4 contains the filter suggestion for the jungle world. A possible filter A could be ranging from  $0.6\mu\text{m} \leq \lambda \leq 0.7\mu\text{m}$ . The sharp rise in surface reflectance around  $0.7\mu\text{m}$  by the VRE causes a significant change of flux in between the filters A and B.

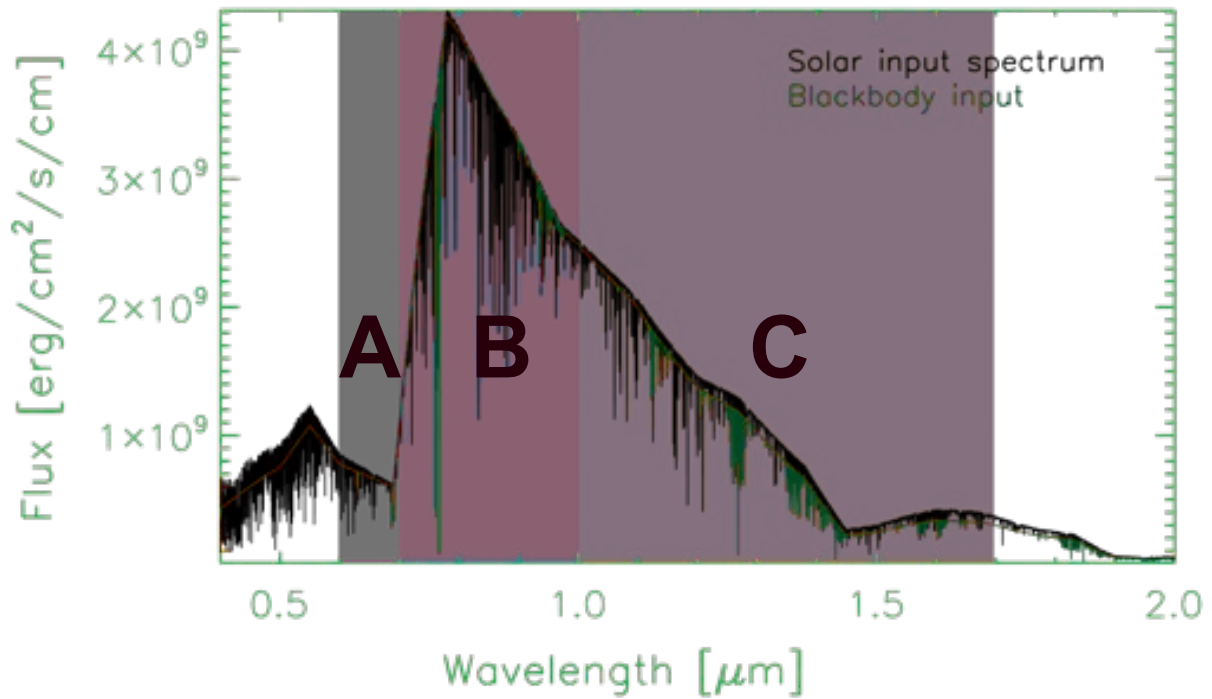


Figure 6.4: *The jungle worlds VRE, overlaid by the model filters A,B and C as described in table 6.1.*

---

# Chapter 7

## SUMMARY & OUTLOOK

The results confirm that the one dimensional spherically symmetric model is a good way to model exoplanets of Earth sizes or larger. This applies for objects with optically thick atmospheres as well as for the optically thin ones. The core work of this thesis consisted in the implementation of a new lower boundary condition that represents a solid surface. This new lower boundary had to allow a partial reflection and absorption of the incoming radiation. This works for surface types with constant, wavelength dependent and angular dependent albedos. Exoplanets with different atmospherical compositions have been simulated. Most of these models converge, although some compositions are not easy to archive, e.g. a martian like atmosphere.

I chose to model different individual scenarios instead of taking a systematic approach, to cover and test all the modifications that had been added to the PHOENIX code. Although there might be numerical problems in individual cases, I can summarize that a wide parameter space of exoplanets with different surfaces and atmospheric compositions can be simulated.

For Earth-like exoplanets with optically thin atmospheres, that are covered by a single surface type only, the surface signal can be seen in the reflected light at visible and near infrared wavelengths. The most dominant surface feature is provided by the vegetation red edge.

The future belongs to the expansion into three dimensions. This way more realistic calculations can be performed. This involves the mapping of the surface with regions of different reflectivities. For an Earth twin this implies that land masses and oceans, clouds, deserts and vegetated surfaces can be mapped and simulated in a single run.

The 3D model also opens up a range of possibilities for the atmospheric composition. This could involve further modifications to the lower boundary in terms of the chemical composition. This way it might be possible to add e.g. oxygen produced by the biosphere.

Although there are lots of benefits resulting from 3D calculations, the 1D models advantages are speed and a lower requirement of computational resources. This is true especially for the optically thin objects, where convergence is reached within a few hours if started from scratch.

Exoplanets within the habitable zone around M stars are interesting targets. The model should be used to characterize a wider variety of exoplanets that are of Earth-sizes or larger, but it would also be very interesting to apply it on potentially habitable moons.

# Bibliography

- Barman, T. S., Hauschildt, P. H., & Allard, F. 2001, *The Astrophysical Journal*, 556, 885
- Bean, J., Miller-Ricci Kempton, E., & Homeier, D. 2010, *Nature*
- Chandrasekhar, S. 1960, Dover Publications Inc, 393
- Cockell, C. S., Kaltenegger, L., & Raven, J. A. 2009, *Astrobiology*, 9, 623
- Des Marais, D. J., Störzer, H., & Baron, E. 2001, JPL Publication 01-008
- Evans, D. L., Farr, T. G., & Adams, J. B. 1982, in *Lunar and Planetary Science Conference Proceedings*, Vol. 12, *Lunar and Planetary Science Conference Proceedings*, ed. R. B. Merrill & R. Ridings, 1473–1479
- Grenfell, J. L., Stracke, B., von Paris, P., et al. 2007, *Planetary and Space Science*, 55, 661
- Hauschildt, P. H., Barman, T., & Baron, E. 2008, *Physica Scripta Volume T*, 130, 014033
- Hauschildt, P. H., Barman, T. S., Baron, E., & Allard, F. 2003, in *Astronomical Society of the Pacific Conference Series*, Vol. 288, *Stellar Atmosphere Modeling*, ed. I. Hubeny, D. Mihalas, & K. Werner, 227–+
- Hauschildt, P. H., Störzer, H., & Baron, E. 1994, *Journal of Quantitative Spectroscopy and Radiative Transfer*, 51, 875
- Kaltenegger, L., Fridlund, M., & Kasting, J. 2002, in *ESA Special Publication*, Vol. 514, *Earth-like Planets and Moons*, ed. B. H. Foing & B. Battrock, 277–282
- Kaltenegger, L., Jucks, K., & Traub, W. 2006a, in *IAU Colloq. 200: Direct Imaging of Exoplanets: Science & Techniques*, ed. C. Aime & F. Vakili, 259–264
- Kaltenegger, L. & Selsis, F. 2009, ArXiv e-prints

## BIBLIOGRAPHY

---

- Kaltenegger, L. & Traub, W. A. 2009, *apj*, 698, 519
- Kaltenegger, L., Traub, W. A., & Jucks, K. W. 2006b, in *Bulletin of the American Astronomical Society*, Vol. 38, *Bulletin of the American Astronomical Society*, 1228–+
- Kasting, J. F. 1993, *Science*, 259, 920
- Kasting, J. F. & Catling, D. 2003, *Annual Review of Astronomy and Astrophysics*, 41, 429
- Kasting, J. F., Whitmire, D. P., & Reynolds, R. T. 1993, *Icarus*, 101, 108
- Lammer, H., Hanslmeier, A., Schneider, J., et al. 2010, *Solar System Research*, 44, 290
- Leger, A., Mariotti, J. M., Mennesson, B., et al. 1996, *Icarus*, 123, 249
- Lineweaver, C. H., Fenner, Y., & Gibson, B. K. 2004, *Science*, 303, 59
- Lucy, L. B. 1964, *SAO Special Report*, 167, 93
- Meadows, V. S. 2006, in *IAU Colloq. 200: Direct Imaging of Exoplanets: Science & Techniques*, ed. C. Aime & F. Vakili, 25–34
- Mihalas, D. 1978, San Francisco: W. H. Freeman & Company
- Mullen, L. 2010
- Nutzman, P. & Charbonneau, D. 2008, *Astronomical Society of the Pacific*, 120, 317
- Olson, G. L. & Kunasz, P. B. 1987, *jqsr*, 38, 325
- Rutten, R. J. 2003
- Schrag, D. P., Berner, R. A., Hoffman, P. F., & Halverson, G. P. 2002, *Geochemistry, Geophysics, Geosystems*, 1
- Seager, S., Turner, E. L., Schafer, J., & Ford, E. B. 2005, *Astrobiology*, 5, 372
- Seager, S., Whitney, B. A., & Sasselov, D. D. 2000, *Astrophysics Journal*, 540, 504
- Segura, A., Krelow, K., Kasting, J. F., et al. 2003, *Astrobiology*, 3, 689
- Selsis, F. 2002, in *ESA Special Publication*, Vol. 514, *Earth-like Planets and Moons*, ed. B. H. Foing & B. Battrick, 251–258

Spiegel, D. S., Menou, K., & Scharf, C. A. 2008, 681

Swain, M. R., Vasisht, G., & Tinetti, G. 2008, ArXiv e-prints

Tinetti, G., Cash, W., Glassman, T., et al. 2009, in *Astronomy*, Vol. 2010, astro2010: The Astronomy and Astrophysics Decadal Survey, 296–+

Vogt, S. S., Butler, R. P., Rivera, E. J., et al. 2010, *Astrophysical Journal*, 723, 954

Wiscombe, W. J. & Warren, S. G. 1980, *Journal of Atmospheric Sciences*, 37, 2712

Wolstencroft, R. D. & Raven, J. A. 2002, *Icarus*, 157, 535

## ACKNOWLEDGEMENTS

Ich möchte an allererster Stelle meinen Eltern danken, die mich immer unterstützt haben. Dann natürlich meinem Doktorvater Prof. Peter Hauschildt für die gute Zusammenarbeit. Und der ganzen Arbeitsgruppe Theorie, mit denen die Arbeitszeit noch viel netter war, besonders Veronica Arias. Generell danke ich allen wissenschaftlichen Mitarbeitern für den Austausch, dort wo er stattgefunden hat, und den lieben Menschen aus der Verwaltung.